Geomorphology 474 (2025) 109641

Contents lists available at ScienceDirect

Geomorphology

journal homepage: www.journals.elsevier.com/geomorphology

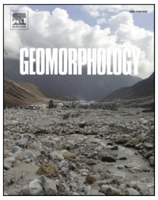

Formation and evolution of grus deposits in the Çine Submassif, Southwest Türkiye: A multi-proxy approach

Murat Gül [a,b,*], Ceren Küçükuysal [b,c], Göksu Uslular [d], Gerald Raab [e], Markus Egli [f]

[a] Department of Civil Engineering, Muğla Sıtkı Koçman University, 48100 Muğla, Turkey
[b] Department of Geological Engineering, Muğla Sıtkı Koçman University, 48100 Muğla, Turkey
[c] Natural and Engineered Geomaterials Laboratory, Research Laboratory Center, Muğla Sıtkı Koçman University, Muğla, Turkey
[d] Polar Research Institute, TÜBİTAK Marmara Research Center, 41470 Gebze, Kocaeli, Turkey
[e] Department of Earth and Environmental Sciences, Dalhousie University, Oxford Street, Halifax 1459, Canada
[f] Department of Geography, University of Zurich, 8057 Zurich, Switzerland

ARTICLE INFO

Keywords:
Grus deposits
Granitic landforms
Weathering indices
Sediment geochemistry
Çine submassif

ABSTRACT

Grus deposits may be a key element in deciphering the evolution of granitic landforms due to their rapid formation, sensitivity to environmental factors, and influence on landscape morphology. This study explores the mineralogical, geochemical and structural characteristics of grus deposits developed on granitoid bedrock through subsurface weathering in a semiarid region, the Çine submassif (SW Türkiye), focusing on how topography, mineral composition and climate affect their formation and spatial variability. Two distinct grus types were identified: thinner (0–20 cm), homogenous, sand-rich deposits on upper slopes, and thicker (40–100 cm), heterogenous, gravel-rich layers in the valley and downslope near bedrock outcrops. The bimodal grain-size distributions among grus types may reflect progressive weathering along topographic gradients, where upper slopes experience limited weathering due to reduced water retention and steeper gradients, leading to the formation of thinner, sand-rich deposits. In contrast, downslopes and valleys allow for prolonged water infiltration and feldspar breakdown, resulting in thicker, gravel-rich deposits with a more advanced weathering profile. Grus consists primarily of quartz, albite, orthoclase and mica, with accessory clay minerals such as kaolinite. Geochemical data indicate a felsic grus composition with limited variations, high Chemical Index of Alteration (CIA) values (59 to 69 %), and a gradual weathering trend towards kaolinite, driven by feldspar weathering and fluctuating water infiltration along slopes.

The Principal Component Analysis (PCA) highlights chemical composition and grain size as key parameters differentiating grus types. The interplay of topography, water dynamics, and local structural and mineralogical characteristics controls both the formation and weathering intensity of grus, with variations in deposit characteristics reflecting the influence of slope position and water infiltration on weathering process. These findings provide new insights into granitoid landform evolution, while further geochronological studies are recommended to clarify the temporal evolution of grus mantles and subsurface weathering features across the region.

1. Introduction

Subsurface weathering is a fundamental geomorphological process that transforms bedrock into regolith, affecting landscape evolution by driving erosion, soil formation and long-term topographic changes (Le Pera and Sorriso-Valvo, 2000; Dixon and von Blanckenburg, 2012; Migoń, 2022). This process is also critical to the biogeochemical cycling of elements, as it releases essential nutrients such as calcium, magnesium and potassium from minerals, which contribute to soil fertility and carbon sequestration, and play a key role in regulating atmospheric CO_2 over a geological timescale (Brantley and Lebedeva, 2011; Navarre-Sitchler et al., 2015; Raab et al., 2017; Goodfellow and Hilley, 2022). This transition from bedrock to regolith involves physical fragmentation and chemical decomposition, the rates and dynamics of which vary depending on environmental conditions.

In granite landforms, subsurface weathering can yield diverse geomorphological features, from large-scale landforms such as inselbergs, tors and bornhardts to smaller-scale features like tafoni, grus

---

[*] Corresponding author at: Department of Civil Engineering, Muğla Sıtkı Koçman University, 48100 Muğla, Turkey.
E-mail address: muratgul@mu.edu.tr (M. Gül).

https://doi.org/10.1016/j.geomorph.2025.109641
Received 18 July 2024; Received in revised form 29 January 2025; Accepted 29 January 2025

deposits and honeycomb weathering (Twidale, 1986, 1997; Campbell and Twidale, 1995; Darmody et al., 2008; Migoń and Vieira, 2014). Grus, forms through weathering of granitoids and other coarse crystalline rocks, giving rise to the formation of a coarse-grained material (sand + gravel 75–100 %; silt + clay <25 %; clay <10 %; Migoń, 1997). The variability of grain sizes reflects differences in weathering intensity and rock composition (Migoń, 1997; Migoń and Thomas, 2002; Hayes et al., 2020; Goodfellow and Hilley, 2022). Grus is also distinguished by its granular texture, quartz and K-feldspar-rich composition and high permeability (Migoń, 1997; Migoń and Thomas, 2002). The permeability and porosity of weathered rocks, which are controlled by structural features, play a key role in fluid transport during subsurface weathering, which in turn govern the development of features like tors and tafoni (Twidale, 1986; Hayes et al., 2020). Factors such as water flux, climate (e.g., precipitation and temperature patterns), mineral size and composition (e.g., the presence of biotite), and jointing contribute to grus formation, making its development highly sensitive to environmental variations (Twidale, 1986; Kanamaru et al., 2018; Shen et al., 2019; Xu et al., 2022; Goodfellow and Hilley, 2022).

The Çine submassif, located in the southern part of the Menderes Massif in SW Türkiye, comprises an orthogneiss core and a phyllite-schist-marble cover (Bozkurt and Oberhänsli, 2001; Bozkurt, 2004; Régnier et al., 2007; van Hinsbergen, 2010; Koralay et al., 2012) (Figs. 1A-C). This region displays various subsurface and spheroidal weathering products (e.g., tor, inselberg, and tafoni; Alkanoğlu, 1984; Gül and Uslular, 2016), formed in response to its geodynamic, paleoclimatic and the recent Mediterranean environmental conditions (Gessner et al., 2013; Gül and Uslular, 2016; Ocakoğlu, 2020). While grus deposits, which are a key outcome of subsurface weathering in granitic and gneissic landforms, are documented in the region (Gül and Uslular, 2016), the specific processes governing their formation, distribution and geochemical characteristics remain poorly understood. Grus deposits in the Çine submassif are of particular interest because their formation is controlled by the region's Mediterranean climate and its unique geological setting, characterised by a granitoid composition and structural features shaped by active tectonics. However, no studies to date have sufficiently investigated the mechanisms behind the spatial variability of grus here, nor have they examined how these deposits relate to the broader geomorphological evolution of the region.

This study addresses these gaps by conducting an in-depth analysis of the grus formation in the Çine submassif (Fig. 1D-F). We intend to determine the degree of weathering and its controlling factors using grain-size distribution, mineralogical and geochemical analyses. By reconstructing weathering processes and analysing the spatial distribution of grus in the region, this study contributes to a more comprehensive understanding of subsurface weathering dynamics, particularly the interplay between physical disintegration and chemical alteration.

2. Study area

The Menderes Massif is a NE-SW trending metamorphic core complex in western Anatolia, tectonically overlain by the Lycian Nappes in the south and the İzmir-Ankara-Erzincan Suture in the north (Figs. 1A and B). The E-W trending grabens (Gediz, Küçük and Büyük Menderes), which are seismically active, separate the massif into the northern, central and southern (Çine) submassifs (Şengör et al., 1984; Bozkurt et al., 1995; Bozkurt and Oberhänsli, 2001; Candan et al., 2001) (Fig. 1B). The region has been subjected to two main metamorphic episodes: the regional HT/MP Barrovian-type in the Eocene (i.e., the main Menderes metamorphism) and the subsequent greenschist retrograde

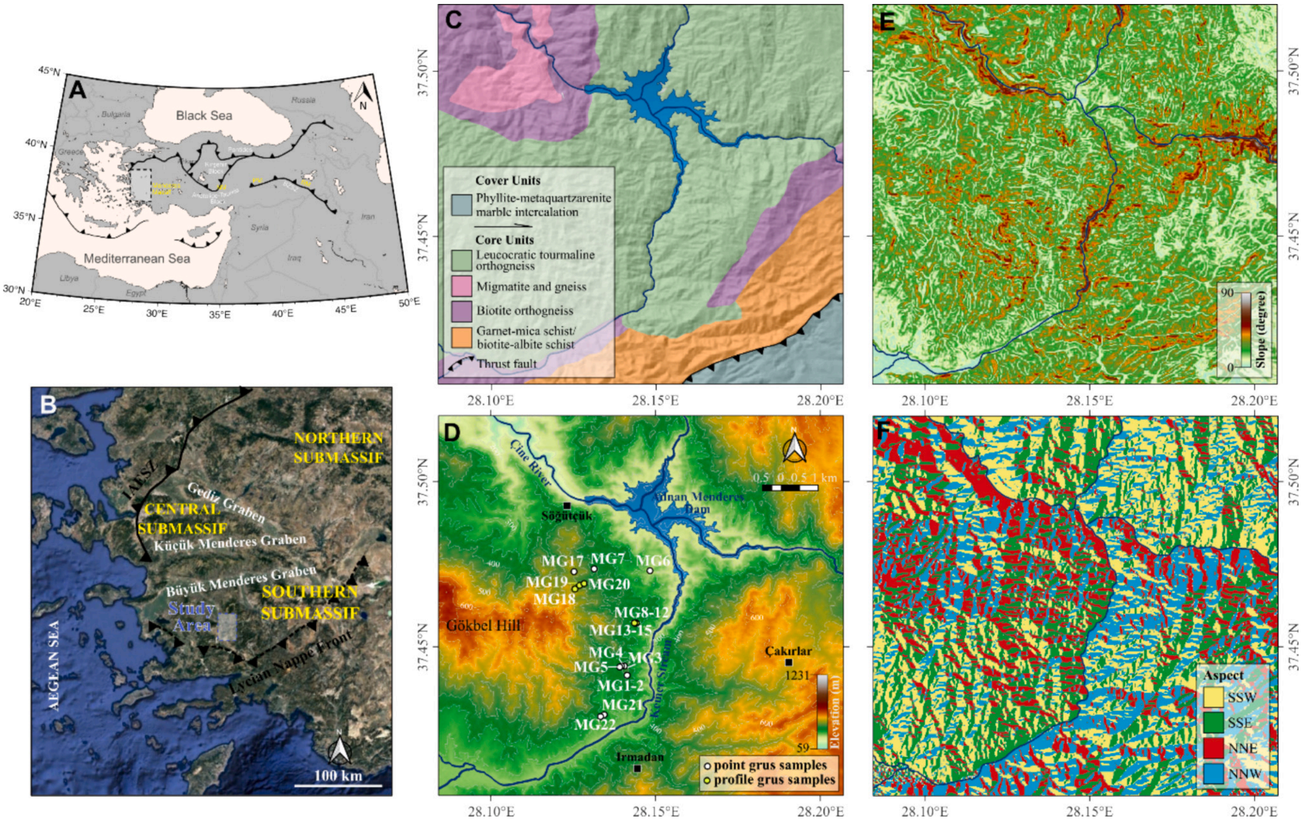

Fig. 1. Overview of the study area and geological context. A. The inset map of Turkey displays the main tectonic structures and massifs (BM: Bitlis massif, PM: Pötürge massif). The white rectangle indicates the area of B. The southwestern region of Anatolia hosts the different core complexes (northern, central, and southern) of the Menderes Massif. The study area is presented in C—F. C. Geological map of the study area (modified after MTA and Koralay et al., 2012). D. Coloured digital elevation model (30 m-resolution ALOS3D DEM; (Tadono et al., 2015) of the study area shows the sampling locations (point sampling represents the top grus, while profile sampling includes both top and bottom grus samples). E-F. Slope and aspect maps were derived from the ALOS3D DEM.

metamorphism during the Miocene (Bozkurt and Oberhänsli, 2001; Whitney and Bozkurt, 2002; Bozkurt, 2004; Rimmelé et al., 2005). These are related to the southward movement of the Lycian Nappes (ophiolites, accretionary prisms, volcanosedimentary units, and sedimentary rocks) and the exhumation of the massif along the currently low-angle normal faults (Şengör et al., 1984; Collins and Robertson, 1997; Gürer and Yılmaz, 2002; Bozkurt, 2004; Koralay et al., 2012). The region has been under the effects of extension since the late Miocene (Bozkurt, 2001; Westaway et al., 2003) together with the regional uplift (0.1–0.3 mm/yr; Westaway et al., 2003, 2004).

The Çine submassif, located in the southern sector of the Menderes massif, consists of core units (Upper Proterozoic metasediments, mica schist, orthogneiss, metagabbros, and metanorite intrusions) and cover units (Paleozoic-Lower Tertiary platform carbonates, marl, clayey limestone and marble) (Candan et al., 2001; Özer et al., 2001; Bozkurt, 2004) (Fig. 1B and C). There are various orthogneisses in the Çine submassif (e.g., leucocratic tourmaline orthogneiss, biotite orthogneiss; Koralay et al., 2012). Subaerial and spheroidal weathering (e.g., Twidale, 1997; Darmody et al., 2008; Migoń and Vieira, 2014) have been widely observed in the Çine submassif (Alkanoğlu, 1984; Gül and Uslular, 2016). Typical geomorphological features of such weathered rocks in the region are inselbergs, tors, tafoni and honeycomb structures (Gül and Uslular, 2016) (Fig. 2). Widespread grus deposits are also evident in the region (Gül and Uslular, 2016), which are the main focus of this study.

The paleoclimatological conditions in the region were subtropical during the Miocene, a period marked by continental warming across Anatolia (e.g., Akgün et al., 2007; Kayseri and Akgün, 2010; Kayseri-Özer, 2013; Jiménez-Moreno et al., 2015; Ocakoğlu, 2020). Through the Pliocene, the region's climate became cool and arid, followed by the beginning of Mediterranean-type climatic conditions characterised by summer droughts (Jiménez-Moreno et al., 2015 and references therein). Today, the Çine submassif still experiences a Mediterranean climate, with annual mean temperatures of ~15.2 °C (Muğla Province) and ~16.4 °C (Yatağan district) and an annual precipitation of 1135 mm and 649 mm, respectively (Mersin et al., 2022). Despite the moderate amount of annual precipitation, there are no perennial streams or springs in the sampling area. Dry creek beds, directed NS and NE, connect to the Kemer Stream (Fig. 1D). The stream beds in the study area consist of weathered granitoid material rather than bedrock, indicating active subsurface processes (Gül and Uslular, 2016). The absence of perennial streams that set a base level for weathering, probably facilitates deep weathering processes below stream bed levels. Evidence for this includes the preserved weathering profiles and in-situ grus mantles observed creek beds and downslope areas, where water percolation dominates over surface runoff. This promotes the continued formation

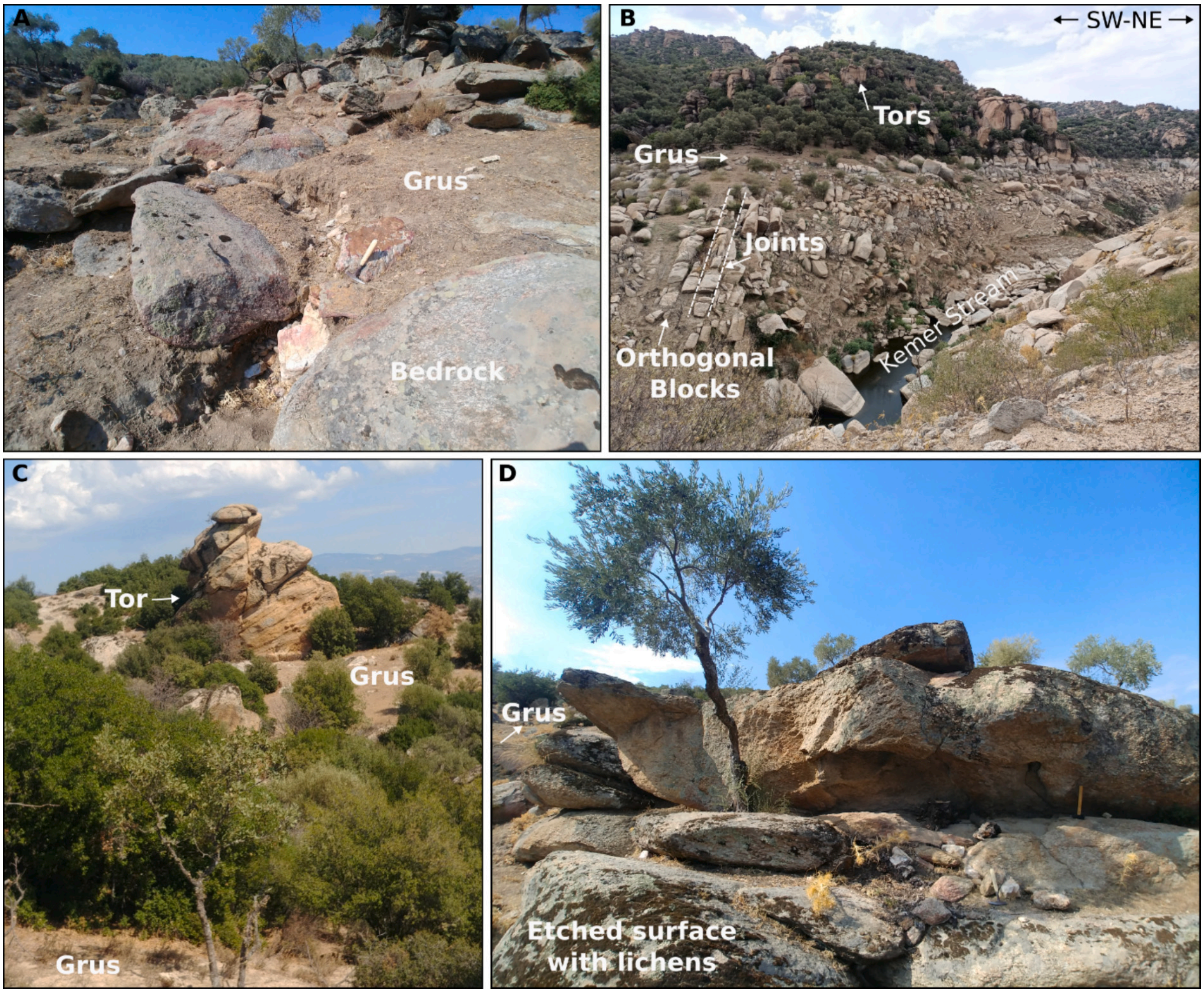

Fig. 2. General overview of sub-surface weathering products including grus, patchy soils, and vegetation. A. Orthogneiss blocks at upper hills are surrounded mainly by thin (8–20 cm) grus layers (hammer for scale: 33 cm; sample MG-21, Fig. 1D). B. Orthogonal blocks display jointing and colour variations due to seasonal water level changes in the dam lake of the Kemer Stream that borders the eastern part of the study area (southeast of the sample MG-1-2, Fig. 1D). Grus layers are visible between the intersections of orthogonal blocks and tors. C. A tor consisting of orthogneiss, surrounded by grus deposits (samples MG-1-2 and MB-1, Fig. 1D). D. Orthogneiss blocks with etched surfaces caused by the formation of lichens on sheeting joints (hammer as a scale: 33 cm; located at the MB-4 sample site in Fig. 1D).

and preservation of weathering products (Gül and Uslular, 2016).

The complex metamorphic and tectonic evolution of the Çine submassif, combined with distinct paleoclimatological and environmental conditions, is thought to be a primary driver of subsurface and spheroidal weathering in the region (Gül and Uslular, 2016). While the presence of grus formations is noted by Gül and Uslular (2016), there remains a gap in understanding the detailed characteristics of these deposits and their specific relationships to parent rock types, weathering processes, and influencing environmental factors. This lack of comprehensive information limits our ability to fully interpret the geomorphological and geochemical dynamics in grus formation within the Çine submassif.

3. Methodology

3.1. Sampling

Grus samples were collected from the southwestern part of the Çine submassif to investigate weathering patterns and mineralogical variations within the study area, consisting predominantly of leucocratic tourmaline orthogneiss (Figs. 1C-F and 2). A total of 35 grus samples were taken, representing different topographic and slope conditions to ensure spatial coverage. The sampling points, either at upper hills or valleys, were consistently selected as close as possible (1–2 m) to the tors to minimise transportation effects and ensure that the grus samples represented the local material. Tors are usually located on ridge crests, where physical and chemical weathering processes operate directly on the underlying bedrock, producing grus in situ. By sampling the uppermost layer (0–15 cm; hereafter top grus), we aimed to capture the material most recently produced through bedrock weathering, with minimal influence from downslope transport or external inputs (Fig. 1D). In addition, vertical grus profiles were opened at five selected sites, and both the top (0–15 cm) and the bottom layers (15–40 cm; hereafter bottom grus) were sampled (Figs. 1D and 3A-B). This approach allowed us to examine vertical changes in grain size, mineral content, and weathering intensity, which can reveal subsurface weathering processes and help quantify the progression of chemical weathering. At each site, the maximum and average grain sizes of the grus material were also measured to understand the mechanical breakdown of the parent rock. Parent rock samples ($n = 20$) were also taken (Fig. 2) to evaluate their petrographical characteristics and determine the primary minerals susceptible to weathering, providing a baseline for comparing the weathering products in the study area.

3.2. Granulometric analyses

The grus samples were dried and sieved from -5Φ to 5Φ with 1Φ intervals) to determine the grain size distribution and sediment characteristics, such as sorting, skewness, kurtosis and compositional properties, which are key indicators of weathering intensity and transport processes. Statistical analyses of the sieving results (e.g., mode, median, kurtosis and skewness) were performed by using the GRADISTAT MS Excel Macro (Blott and Pye, 2001) to classify the sediments according to Folk's classification scheme (Folk, 1954). This classification helped us understand the sorting of the grus, providing insight into depositional processes and the degree of mechanical breakdown of the parent rock. The samples were also grouped by grain size parameters: sorting (very well sorted, well sorted, moderately sorted, poorly sorted and very poorly sorted), skewness (extremely coarse skewed, coarse skewed, nearly symmetrical, fine skewed and extremely fine skewed), and kurtosis (very platykurtic, platykurtic, mesokurtic, leptokurtic and very leptokurtic). To analyse the chemical and mineralogical composition, the bedrock and grus samples were ground to a fine powder for further major and trace element analyses. For XRD analyses, particles with a diameter of <63 μm were selected to ensure optimal detection of clay and secondary minerals formed during the weathering process.

3.3. Mineralogical, petrographical and geochemical analyses

Twenty thin sections of orthogneiss bedrocks were prepared at the General Directorate of Mineral Research and Exploration of Türkiye (MTA) to characterise the parent rock of the grus samples. These thin sections were examined under a polarised microscope to identify the main mineral assemblages and textures.

X-ray Diffraction (XRD) analyses were carried out at the MTA laboratories to identify the minerals in the samples. A Panalytical Expert Pro diffractometer, equipped with a Cu tube at 40 kv and 30 mA current, was employed at a scan rate of 2°/min. Diffractograms for bulk samples were scanned in the 4–70° (2Θ) range. The clay fraction was separated by sedimentation and centrifugation. The fine fractions were prepared as oriented slides in four conditions: (i) air-dried, (ii) saturated with ethylene glycol, and heated to (iii) 300 °C and (iv) 550 °C to identify the clay minerals present in the samples. The oriented samples were analysed by XRD in the range of 2–42° (2Θ). Mineral identification was done according to Thorez (1976), Chen (1977) and Moore and Reynolds (1989). A semi-quantitative estimate of the minerals was done according to Brindley (1980), by using the mineral intensity factors from Boski et al. (1998)and Fagel et al. (2003) for bulk samples and from (Biscaye, 1965) for the clay fraction.

Grus samples were examined by a Field Emission-Scanning Electron Microscope (FE-SEM) at the Advanced Technology Application and Research Center, Pamukkale University, Denizli, Türkiye. This analysis was performed with an accelerating voltage of 0.02–30 kV, and was conducted to identify the micromorphology of the minerals, which provides insights into surface weathering features, mineral dissolution patterns, and secondary mineral formation. Elemental characterisation of these minerals was done using energy-dispersive X-ray spectrometry (EDX) to determine the chemical composition of individual mineral grains, enabling the identification of weathering-induced elemental changes and the detection of newly formed weathering products.

The grus samples were powdered to <75 μm to ensure homogeneity and improve the accuracy of geochemical analyses. The major oxide compositions were measured with Inductively Coupled Plasma Atomic Emission Spectroscopy (ICP-AES) after fusion, providing a detailed profile of the primary mineral components essential for understanding weathering intensity and mineral stability. Trace and rare earth elements were identified by Inductively Coupled Mass Spectrometry (ICP-MS) following acid decomposition (5 % of HNO_3), as these elements provide insight into geochemical processes such as element mobility, provenance and subtle weathering trends. Loss on ignition (LOI) values were measured at 1000 °C to quantify the weight loss related to the release of volatile contents, offering a proxy for weathering degree and the presence of secondary weathering products.

3.4. Weathering indices

Mineralogical and geochemical fingerprints in weathering products are essential indicators of past climatic and environmental conditions. They record changes in temperature, precipitation, and vegetation over time (Sheldon and Tabor, 2009), influencing mineral's susceptibility to weathering. For example, specific elemental depletions and mineral transformations in weathering profiles can reveal historic variations in chemical weathering intensity, which are directly influenced by climate. We applied a combined mineralogical and geochemical approach to better understand these processes and quantify the extent of chemical weathering.

One of the primary indices used is the “Chemical Index of Alteration (*CIA*)” proposed by Nesbitt and Young (1982), which is calculated using the following formula (1):

$$\mathrm{CIA} = 100 \text{ x } Al_2O_3/(Al_2O_3 + CaO + K_2O + Na_2O) \tag{1}$$

where all oxide compositions are expressed in molar proportions. The

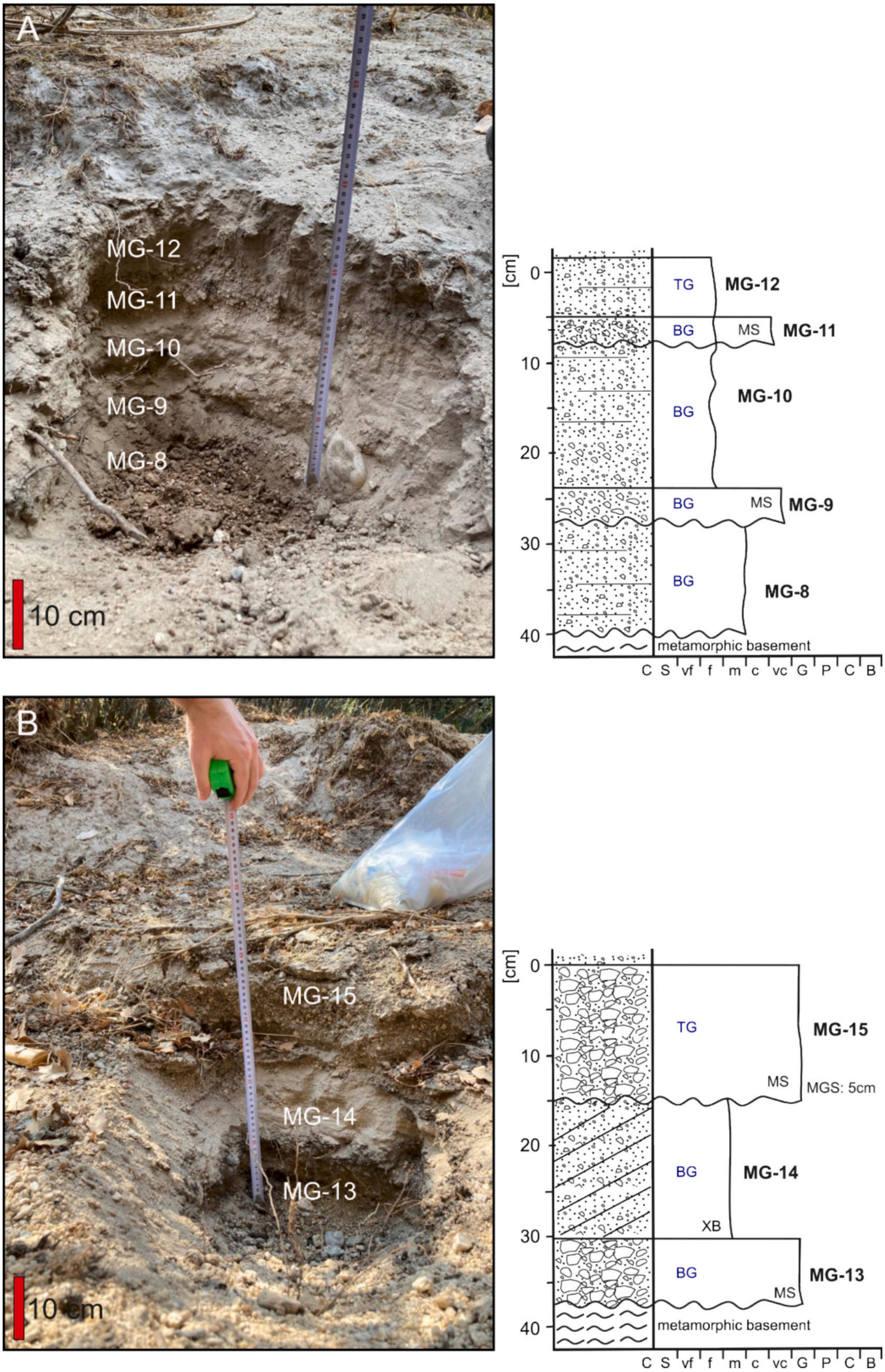

Fig. 3. Pits at the MG-8-12 and MG-13-15 sites. The profiles are from the front of the sidewall and the middle part of the valley (see Fig. 1D for the profile locations). Abbreviations are TG: top grus, BG: bottom grus, MS: matrix-supported, XB: cross-bedded, MGS: maximum grain size, C: clay, S: silt, vf: very fine grained sand, f: fine grained sand, m: medium-grained sand, c: coarse grained sand, vc: very coarse grained sand, G: gravel, P: pebble, C: cobble, and B: boulder.

correction of CaO* in the silicate fraction was performed according to McLennan (1993). This index measures the degree of transformation from primary minerals like feldspar to secondary minerals. The *CIA* values are projected on Al_2O_3-CaO + Na_2O-K_2O (*A-CN-K*) ternary diagrams to predict weathering trends and infer climatic conditions responsible for different levels of feldspar breakdown.

In addition to the CIA, we used the $M^+ - 4Si - R^{2+}$ system (Meunier et al., 2013), which provides insight into mineral transformation processes and the relative mobility of elements during weathering. Here, M^+ refers to the sum of Na^+, K^+ and $2Ca^+$ions, while R^{2+} represents divalent cations ($Mg^{2+} + Fe^{2+} + Mn^{2+}$). The 4Si value indicates the number of Si^{4+} cations divided by 4. The normalised $M^+ - 4Si - R^{2+}$ (%) values were plotted in a ternary diagram to better understand the distribution of these elements during different stages of weathering. Trivalent cations (R^{3+}) were then considered and used to calculate the $R^{3+} / (R^{3+} + R^{2+} + M^+)$ ratio.

Furthermore, the Weathering Intensity Scale (Δ4Si) was calculated using the formula of $[(4Si_{soil} - 4Si_{UCC}) \times 100] / (100 - 4Si_{UCC}) * 100$. Here, the Upper Continental Crust (UCC) represents the unweathered parent rock, with a reference value of 39.8 % for 4Si (Meunier et al., 2013 and references therein). This index helps quantify the extent of Si^{4+} depletion during weathering, ranging from 0 % (unweathered rock) to 100 % (maximum alteration).

In addition to these primary weathering indices, several other geochemical indices were applied to comprehensively understand chemical weathering on grus formation. These indices include the *WIP* (Weathering Index of Parker; Parker, 1970; Price and Velbel, 2003), *CPA* (Chemical Proxy of Alteration; Nesbitt and Young, 1982), *PI* (Product Index; Ruxton, 1968), *SF* (Silica Factor; Jenny, 1942), *SA* (Sodium Alteration; Ruxton, 1968), *SOC* (Sesquoxide Content, Irfan, 1996), *LC* (Leaching Coefficient; Ng et al., 2001), *Si—Ni*, *Kr* (Silica-sesquioxide Ratio; Moignien, 1966), *MWPI* (Modified Weathering Potential Index; Vogel, 1975), *RI* (Recycling Ratio; Garzanti et al., 2014), *R* (Ruxton Ratio; Ruxton, 1968), *VR* (Vogt Ratio; Vogt, 1927), *CIW* (Chemical Index of Weathering; Harnois, 1988), *PIA* (Plagioclase Index of Alteration; Fedo et al., 1995), and *STI* (Silica-Titanium Index; Egli et al., 2008; Raab et al., 2017). The formulas of each index are given in Supplementary Material 1. Each index targets specific aspects of chemical alteration, such as leaching intensity, element mobility and mineral stability. Therefore, the use of multiple indices is necessary because none can capture all aspects of weathering, especially in complex systems like granitic landforms. By employing a suite of weathering indicators, we can better assess the degree of chemical transformation, identify dominant weathering mechanisms, and evaluate the environmental conditions that affected grus formation across the study area.

3.5. *Statistical analyses*

The Principal Component Analysis (PCA) was employed for the major oxide geochemistry of the grus samples to reduce data dimensionality and identify key patterns and relationships between chemical composition and physical sediment characteristics (Pedregosa et al., 2011). The major oxide values were standardised and then transformed into a new set of uncorrelated variables via the centred log ratio (clr) method. The PCA was performed on this transformed data to calculate two main principal components (PCA 1 and PCA 2), representing the majority of the variance in the geochemical data. This enabled us to explore correlations between the geochemical signatures and grain size distributions (sorting, skewness and kurtosis) across different sediment types (top and bottom grus) and classes (sandy gravel—sG and gravelly sand—gS based on Folk's classification). The main purpose of this analysis was to uncover how specific grain size parameters relate to chemical weathering processes, such as the enrichment or depletion of certain oxides during the breakdown and transport of grus material.

In addition, a Genetic Algorithm coupled with a Random Forest Classifier was used to identify the most significant weathering indices affecting sediment characteristics. This approach was implemented using the DEAP (Distributed Evolutionary Algorithms in Python) framework and the "sklearn.ensemble" Python module. The GA was applied to optimise the selection of weathering indices. At the same time, the Random Forest Classifier evaluated their impact on sample types, grain size parameters, and sediment classes based on classification labels derived from the sieving analysis. This method enabled us to determine the indices that best differentiate between sediment characteristics, providing insights into how chemical weathering processes vary between different types of grus and their associated grain size distributions. The accuracy of the classification model was evaluated through cross-validation to ensure robustness and generalisability of the results, which further help in understanding the complex interplay between geochemistry and physical properties in weathering profiles.

4. Results

4.1. *Field characteristics of grus samples*

The grus deposits consisted predominantly of poorly sorted, subangular to angular quartz-bearing grains with a white-cream-glassy appearance. Their thickness varied across the region, mainly depending on the slope (Fig. 1E and F). At topographically elevated positions that were dominated by a steep slope (> 45°; Fig. 1E) pillar structures and boulders (Fig. 2), grus deposits were typically thin (0–20 cm) and homogeneous in texture. However, they were thicker (~40–100 cm and potentially thicker) in downslope areas having a lower slope (< 45°; Fig. 1E) or in depressions and valley bottoms. These latter deposits sometimes displayed a more heterogeneous texture, featuring alternating layers of fine grained and coarse grained material (Fig. 3).

4.2. *Grain-size distributions*

The sieve analysis results given in Supplementary Data S1 categorise the grus samples into two main types based on Folk's (1954) classification: sandy gravel (sG) and gravelly sand (gS) (Fig. 4). These classifications indicate the samples primarily consist of sand and gravel, with mud ratios <4.7 % (Fig. 4). However, there is a significant variation in the proportions of sand and gravel content, ranging from 26.6 % to 96.7 % and 2.8 % to 72.6 %, respectively (Fig. 4). Additionally, alternating layers of coarse and fine materials were observed. The coarsely grained layers are characterised by bimodal, poorly sorted sand gravel (sG) with an average grain size corresponding to fine gravels. In contrast, the fine grained layers consisted of gravelly sand (gS) with an average grain size of medium to coarse sand.

The top and bottom grus samples exhibited key differences in texture and grain size distribution. Both types were generally poorly to very poorly sorted, displaying a bimodal grain size distribution (Fig. 5A). The grain size vs. cumulative weight plot revealed steep curves, characteristic of both grus samples (Fig. 5B). The skewness values for the samples ranged widely from extremely fine- to extremely coarse skewed (Supplementary Data S1). The kurtosis values were mostly platykurtic and very platykurtic, consistent with the observed poor sorting (Supplementary Data S1).

Additionally, the top grus samples generally contained a higher proportion of finer grains, particularly medium to coarse sand, which tended to display an unimodal distribution with right-skewed characteristics. However, the bottom grus samples were composed of relatively coarser material, with a higher content of fine gravels, showing a predominantly bimodal distribution and left-skewed patterns (Fig. 5A). This suggests that the bottom grus layers are slightly more variable in grain size, including both coarser and fine materials, compared to the more uniformly fine-grained top grus layers.

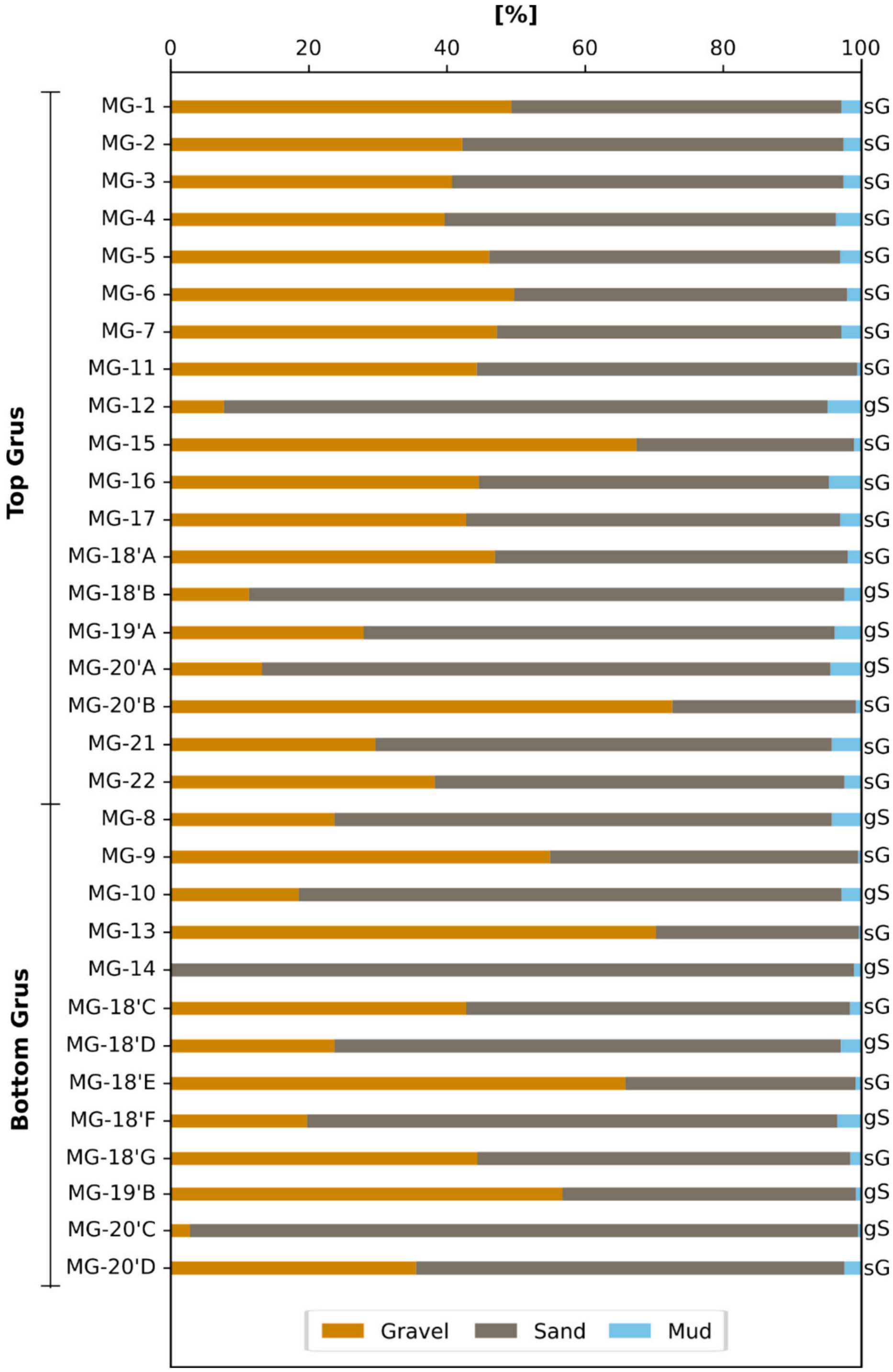

Fig. 4. Gravel, sand, mud (silt + clay) percentages and sediment class (Folk, 1954) of the soil and grus (top and bottom) samples (sG: sandy Gravel; gS: gravelly Sand) (see Supplementary Data S1 for further details).

4.3. Petrographic and bulk geochemical characteristics

Two different types of orthogneiss were identified as potential bedrock (Fig. 6). The first is a leucocratic orthogneiss (leucocratic tourmaline orthogneiss; Fig. 1C) dominated by a granoblastic texture, containing large feldspar (K-feldspar and albite) phenocrysts and biotite and muscovite microphenocrysts showing a lepidoblastic texture. The petrography of the original granite was mainly preserved in this rock. The large feldspars showed a perthitic texture and were primarily altered. Tourmaline and titanite were the accessory minerals. The second orthogneiss (migmatite and gneiss; Fig. 1C) consisted of bands of melanosome, containing biotite and muscovite with a nematoblastic texture and poikiloblastic garnet, and leucosome bands with feldspar (mostly microcline) and quartz microphenocrysts. This rock, which also showed traces of a cataclastic deformation in place, was described as augen-orthogneiss. These petrographic observations agreed with previous studies (e.g., Candan et al., 2011; Gürsu, 2016).

Geochemical analyses of the grus (top and bottom) samples revealed, not surprisingly, a felsic composition with an average SiO_2 content (LOI-free) of 74.1 ± 5.9, 72.5 ± 6.3 and 66.9 wt%, respectively (Table 2).

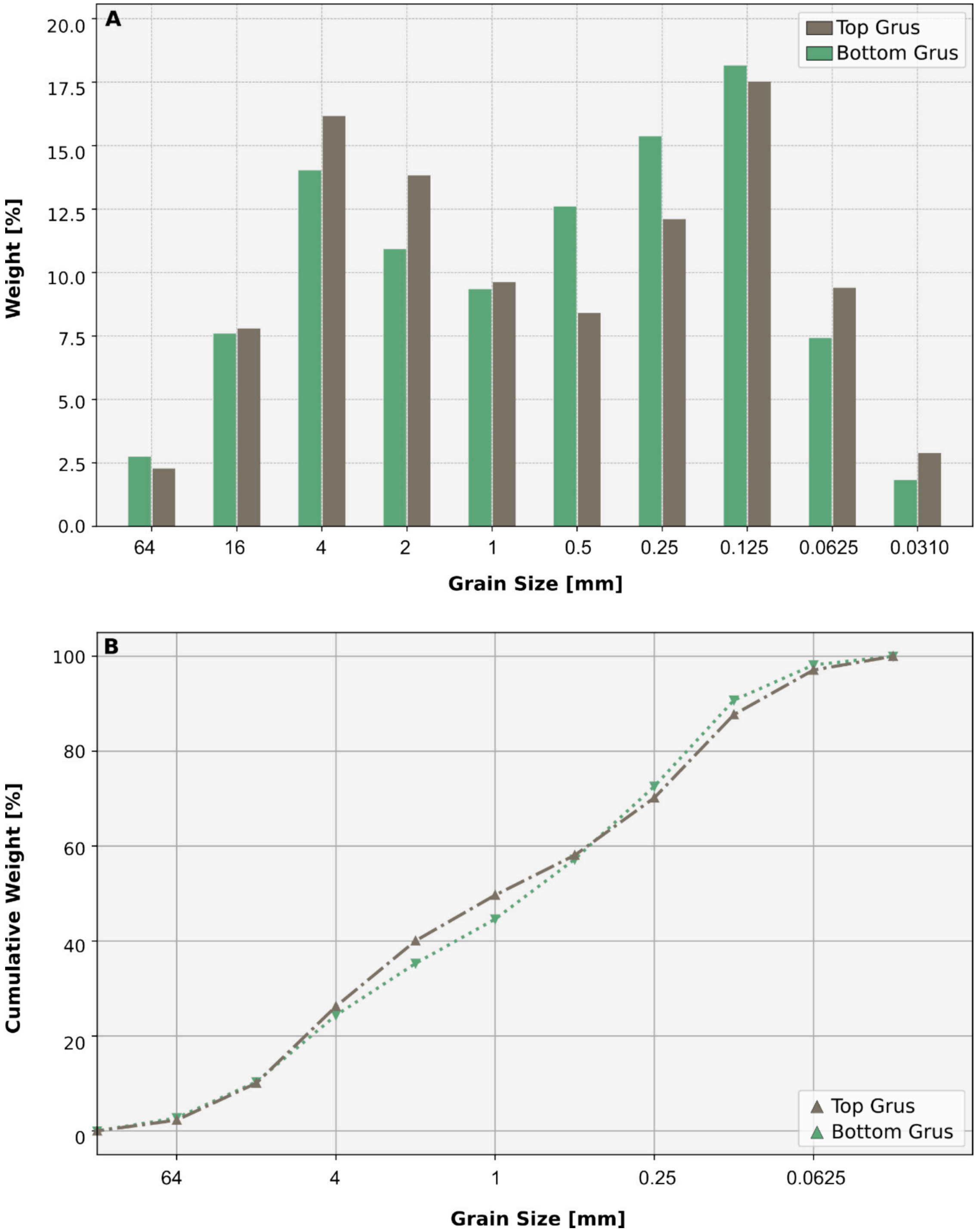

Fig. 5. A. Average grain size distributions and B. Average cumulative weight percentages of soil and grus (top and bottom) samples (see Supplementary Data S1 for further details).

Geochemical variation among the samples was limited, characterised by a high Al_2O_3 content and an alkaline geochemical affinity (Table 2). All geochemical data are provided in the Supplementary Data S2.

The trace element compositions of the samples were lower than the Upper Continental Crust (UCC) composition (Taylor and McLennan, 1985) (Supplementary Data S2). This was particularly valid for some large lithophile elements (e.g., Cs and Ba), high field strength elements (e.g., Zr, Ta, and U), and rare earth elements (e.g., La, Ce, Nd, Sm and Lu).

4.4. *Mineralogical compositions*

In the grus samples, XRD analysis of the bulk material identified albite, orthoclase, quartz, illite/mica and clay minerals (Table 1; Fig. 7). A low-intensity reflection at 0.99 nm, accompanied by a hump reflection at 1.09–1.10 nm in the bulk material diffractogram, indicated the presence of mixed-layer mica/vermiculite. The intensity of these reflections varies with mica and vermiculite content (Fig. 7).

The XRD analysis of the clay fraction further revealed the presence of illite, kaolinite, chlorite, and smectite in the grus samples (Table 1; Fig. 8). Quartz was semi-quantitatively estimated to comprise 12–34 %

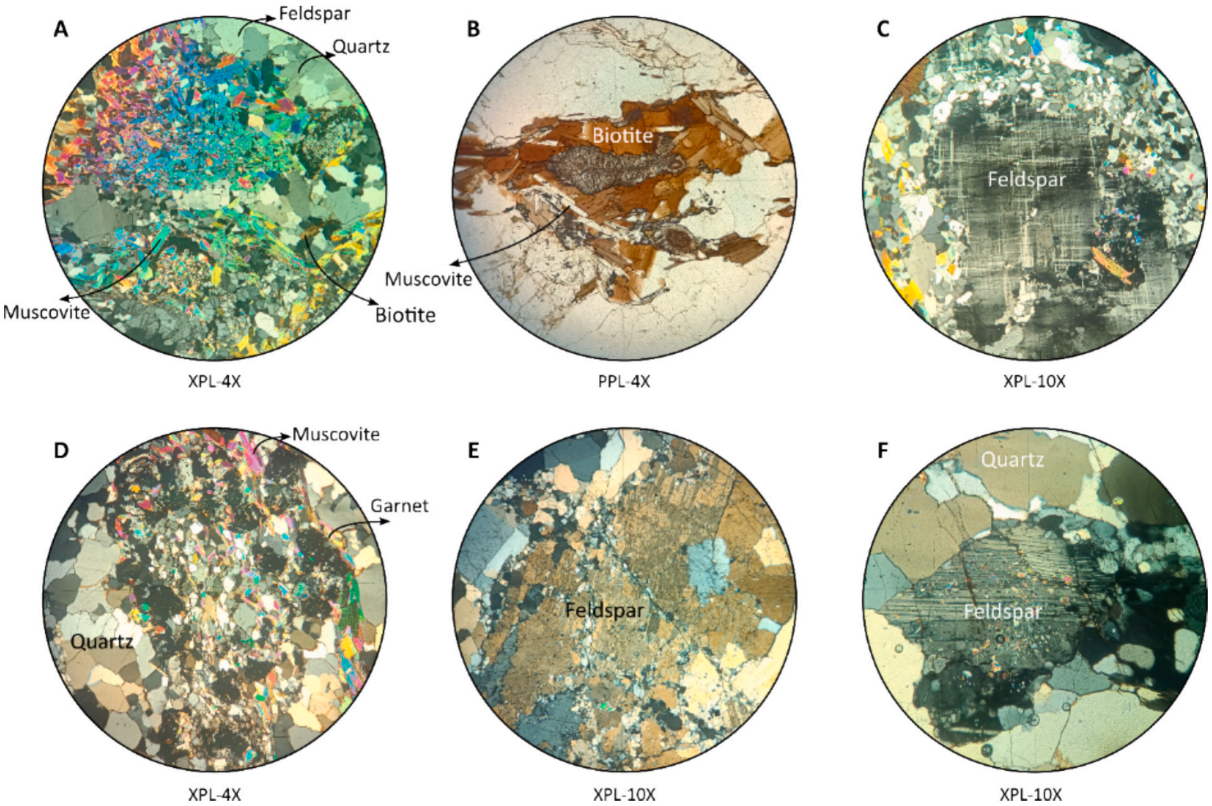

Fig. 6. Photomicrographs of bedrocks A-D. Augen-gneisses with melanosome and leucosome bands, including biotite, muscovite, poikoblastic garnet, feldspar and quartz microphenocrysts, respectively. E-F. Leucocratic orthogneisses were dominated by the granoblastic texture that contained porphyroblasts of perthitic feldspars, biotite, and muscovite microphenocrysts.

Table 1
Semi-quantitative XRD analyses of the bulk material and the clay fraction of the grus samples.

Sample	Bulk			Clay fraction			
	Quartz	Feldspar	Phyllosilicates	Smectite	Illite	Kaolinite	Chlorite
MG-1	18	31	51	0	90	9	1
MG-2	18	59	23	0	94	3	2
MG-3	17	33	50	0	94	5	1
MG-4	16	43	40	0	94	5	2
MG-5	20	45	36	0	93	5	2
MG-6	31	36	33	0	95	3	2
MG-7	22	37	41	0	94	4	2
MG-8-1	19	40	40	<1	92	5	3
MG-9-2	23	30	47	0	94	4	2
MG-10-3	24	57	19	0	95	3	2
MG-11-4	23	77	0	0	98	1	1
MG-12-5	12	56	31	0	98	1	1
MG-13-6	27	46	27	0	98	1	1
MG-14-7	34	66	0	0	100	0	0
MG-15-8	17	44	39	0	97	2	1
MG-16	16	29	54	0	95	3	2
MG-17	15	38	47	<1	94	4	2
MG-18A	27	22	52	0	96	3	1
MG-18B	17	34	50	0	95	3	2
MG-18C	16	34	51	<1	98	1	1
MG-18D	23	33	44	<1	96	3	1
MG-18E	17	55	28	<1	97	2	1
MG-18F	17	44	39	<1	94	3	3
MG-18G	20	40	40	<1	96	3	1
MG-19A	18	40	42	0	98	1	1
MG-19B	32	32	36	0	98	1	1
MG-20A	28	43	29	0	95	3	2
MG-20B	24	38	38	0	98	1	1
MG-20C	33	54	13	0	98	1	1
MG-20D	21	48	31	0	95	4	1
MG-21	30	52	19	0	94	4	2
MG-22	16	58	26	0	95	4	1

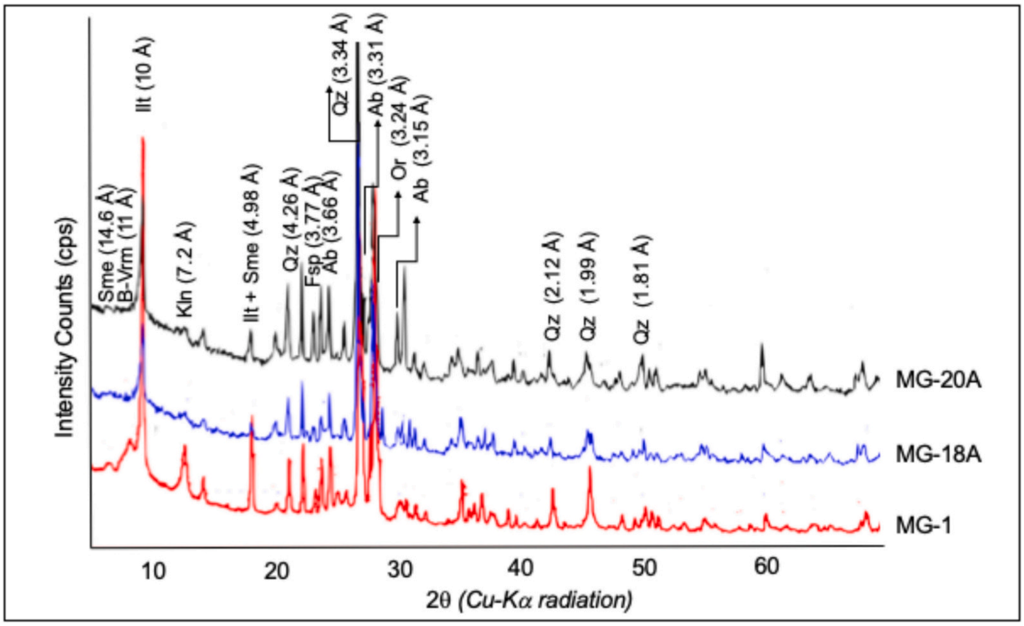

Fig. 7. X-ray diffractograms of the top grus samples (MG-18 A, MG-1 and MG-20 A) (Sme: smectite; Vrm: vermiculite; Bt: biotite; Ilt: illite; Kln: kaolinite; Fsp: feldspar; Ab: albite; Qz: quartz).

of the bulk grus composition. The sum of albite and orthoclase, calculated as total feldspar, exhibited considerable variability, ranging from 22 % to 77 % in bulk samples. The clay minerals, summarised under phyllosilicates, accounted for about 13–54 % of the bulk composition (Table 1). Notably, an inverse relationship was observed between the quantities of feldspar and phyllosilicates in the grus samples, suggesting progressive weathering.

Illite was the most prominent clay mineral in nearly all samples, accounting for about 90–100 % of the clay fraction, except in sample MG-3 (top grus). Smectite was present only in trace amounts (<1 %), while kaolinite and chlorite were identified in low quantities (1–9 % and 1–3 %, respectively). The presence of trace amounts of smectite, which typically forms during the early-stage transformation of biotite and vermiculite, and the limited formation of kaolinite, reflect the constraints such as the composition of weathering fluids or environmental conditions, which could limit the extent of weathering under the present conditions.

4.5. Geochemistry-based weathering indices

All calculated weathering indices are given in the Supplementary Data S2. The CIA values of the bulk samples ranged between 59 and 69, while the profile samples for both MG-18 and MG-20 sequences had index values between 61 and 64. The highest CIA value of 69 in the grus samples indicates that weathering has not yet reached a level that is sufficiently high to fully transform primary minerals into clay minerals or hydroxides.

The CIA values were also projected on the A-CN-K triangular diagram along the A-CN side (Nesbitt and Young, 1984) to visualise weathering trends of the grus material (Fig. 9; Table 2). Most of the grus samples were aligned between a plagioclase-K-feldspar composition, with a slight offset towards Al_2O_3. The weathering of grus showed a slight trend towards the K_2O pole, indicating a potential tendency of illitisation with K^+ addition (Fig. 9; Table 2). However, the interpretation of this trend is ambiguous because of the overlap of the top and bottom grus samples, which may reflect variability in weathering intensity or local geochemical factors affecting the samples. While a trend towards potassium enrichment in the weathering process is evident, the spatial and mineralogical variability of the samples partially overshadows weathering progression.

The M^+- 4Si-R^{2+} system (Meunier et al., 2013) was also used to quantify the Weathering Intensity Scale (WIS) (Fig. 10; Table 2). Calculation of monocationic molar proportions of the major elements and the R^{3+}, R^{2+}, $M^{+,}$ and 4Si parameters are provided in Supplementary Data S2. Unweathered and weathered granite (Meunier, 1980) and granodiorite (White et al., 2003) compositions are displayed as polygons with coloured dotted lines alongside the field of the average composition of felsic rocks (Condie, 1993), together with the illite-quartz, kaolinite-pyrite domain (Meunier et al., 2013) (Fig. 10). The data fall in the unweathered and weathered granite and granodiorite fields with some offsets that are still along the primary weathering trend. Data distribution on the M^+-4Si-R^{2+} ternary plot converged towards the 4Si pole, revealing that chemical weathering proceeded in the direction of kaolinite (Fig. 10). However, the intensity required for altering mica and feldspar into kaolinite, or the enrichment of Si together with leaching of M^+ and partially of R^{2+}, is insufficient. The soil sample was the only one within the illite-quartz domain, showing no K-enrichment (Fig. 10).

4.6. PCA and genetic algorithm results

Fig. 11 displays the PCA results for the top and bottom grus and two soil samples based on various grain size parameters and sample types. The first two principal components (PCA1 and PCA2) collectively account for over 90 % of the total variance, with PCA1 ranging from 57 to 100 % and PCA2 from 0 to 38 % (Supplementary Data S3). There is no clustering among the samples, and the top and bottom grus samples often overlap.

The PCA1 predominantly reflects the impact of chemical composition, specifically showing a negative correlation with SiO_2 across various sample types (ranging from −4 % in EFS to −15 % in ECS samples; Supplementary Data S3) but a positive correlation with Al_2O_3, Fe_2O_3, MgO and CaO (Fig. 11). For example, PCA1 shows strong positive correlation with MgO (~64 %) and CaO (~25 %) in the bottom grus samples, suggesting that these elements are accumulating in chemically weathered environments.

For the top grus samples, PCA1 has a lower negative correlation with SiO_2 (−5 %) and a higher positive correlation with CaO (~53 %) and MgO (63 %), highlighting the role of these oxides in grus formation close

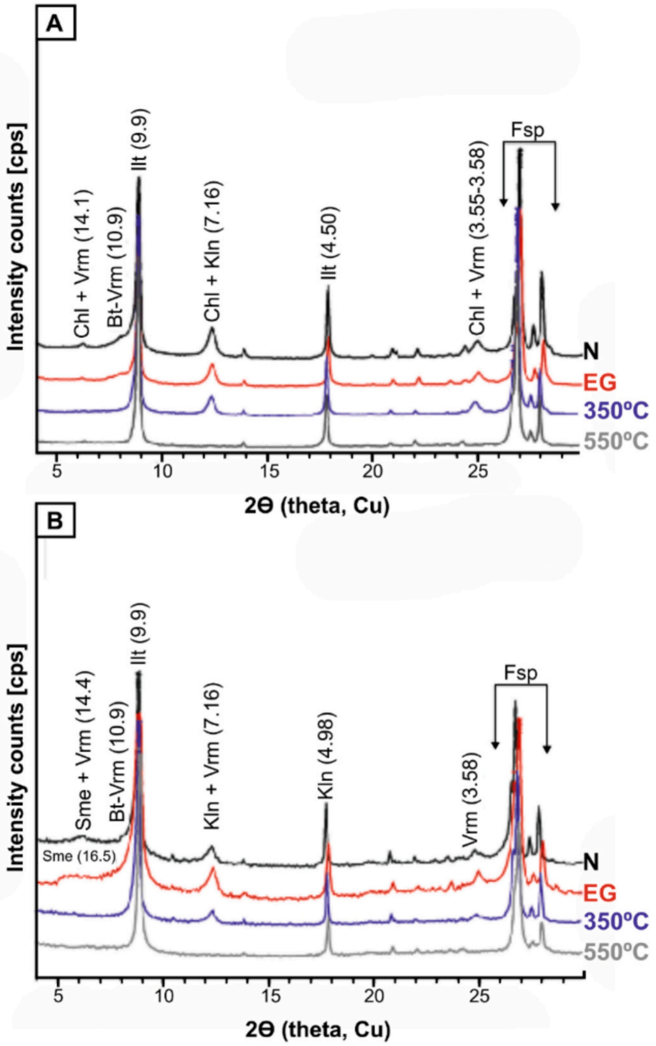

Fig. 8. X-ray diffractograms of the clay fractions of A. the top (MG-1) and B. bottom (MG-18G) grus samples (Sme: smectite; Chl: chlorite; Vrm: vermiculite; Bt: biotite; Ilt: illite; Kln: kaolinite; Fsp: feldspar; N: normal, air-dried clay sample; EG: Ethylene glycol solvated clay sample).

to the surface. Additionally, Na_2O shows a variable correlation with PCA1 across different variables, which are highly correlated to the ECS (~73 %) and moderately correlated in the bottom grus (38 %), suggesting that Na_2O may reflect different stages of weathering in deeper layers.

PCA2 is associated with grain size parameters, including skewness and kurtosis (Fig. 11). Specifically, PCA2 shows a positive correlation with the leptokurtic (L) type (87 % for SiO_2), indicating that sorting and distribution of grains also affect the sample variance along PCA2. Conversely, the negative correlation of PCA1 with the skewness of the coarse (CS) samples indicates that finer, well-sorted material (having a higher SiO_2 content) is characteristic of less-weathered grus.

Using a Genetic Algorithm supported by a Random Forest Classifier, effective weathering indices for sediment characteristics (sample type, grain size parameters, and sediment classes) were identified. Apart from skewness (0.5) and kurtosis (0.6), predictions for other parameters achieved metric scores exceeding 0.8. The CIA emerged as the best representative index overall, while ALK, LC and CIA ranked highest in Folk's classification. Additionally, WIP, SF and CIA were the primary indices that represented samples based on their sorting type.

5. Discussion

5.1. Physical and chemical characteristics of the grus deposits

The Çine submassif has experienced alternating periods of arid and humid climatic conditions since the latest Miocene (Müllenhoff et al., 2004; Akgün et al., 2007; Brückner et al., 2010; Jiménez-Moreno et al., 2015; Ocakoğlu, 2020). This climatic variability (i.e., periodic changes in water availability), concurrent with the exhumation of the massif after unroofing of the Lycian nappes (Gürer and Yılmaz, 2002; Bozkurt, 2004; Koralay et al., 2012; Gürer et al., 2013, and references therein), likely facilitated large-scale and prolonged subsurface weathering in the region (Gül and Uslular, 2016). Upon exhumation and subsequent uplift, surface water exploited zones of weaknesses (i.e., exfoliation cracks), giving rise to thick, deep-subsurface weathering, forming geomorphological features such as boulders, tors, tafoni, etched surfaces and polygonal cracks in the Çine submassif (Gül and Uslular, 2016) (Fig. 12).

The grus deposits observed in the Çine submassif exhibit distinctive variability in both their physical and chemical properties. There is a variation in grus thickness, with thinner (0–20 cm) and homogeneous deposits on upper slopes (> 45°) and thicker (40–100 cm), more heterogeneous deposits in downslope positions and valley bottoms (< 45°; Fig. 12). This suggests that the process of grus accumulation is controlled by both the weathering intensity and the transport processes acting on the grus material (e.g., Buss et al., 2008; Goodfellow et al., 2014). The thicker, more heterogeneous deposits in downslope areas may result from a combination of physiochemical weathering and slower drainage, allowing for more extensive grus accumulation (Goodfellow et al., 2011). Stratigraphic evidence of grus profiles, such as the presence of alternating coarse and fine-grained layers and transitions between poorly sorted deposits, further supports the hypothesis of downslope transport. In contrast, the relatively thin and homogeneous grus deposits at higher elevations contain more uniformly fine grains with unimodal distributions, indicative of a more restricted weathering environment and minimal transport (Fig. 12).

The composition of grus deposits in the study area is dominated by sandy gravel (75–90 %) with a clay content of <10 % (Fig. 4). Top grus samples are finer, showing an unimodal distribution with a higher proportion of sand, while bottom grus samples are coarser and exhibit a bimodal distribution with greater amounts of gravel. This variation highlights both weathering and sorting processes as determining factors on the grain size of the grus deposits. Specifically, the finer, more uniform deposits may be related to areas of more intense weathering and less transport, while the coarser deposits likely reflect more variable transport conditions in downslope regions (Fig. 12).

The weathering indices of felsic grus deposits in the study area, particularly the CIA values ranging from 59 to 69, indicate moderate weathering of the granitoids. This level of alteration, however, is insufficient to generate clay-rich saprolite. The mineralogical data support this conclusion, with illite bearing the dominant clay mineral (accounting for 90–100 % of the clay fraction) and trace amounts of smectite and kaolinite present (Table 1). This mineralogical composition aligns with the parental rock composition (Weber et al., 2012) and indicates that the grus deposits are still in the early to middle stages of weathering, with feldspar and biotite transforming into illite, but not yet progressing to the formation of more weathered minerals such as kaolinite (Figs. 6, 7, and 8). Such characteristics align with the Mediterranean climate in the region (Alçiçek and Jiménez-Moreno, 2013; Jiménez-Moreno et al., 2015; Ocakoğlu, 2020), where seasonal water availability drives episodic weathering and limits secondary clay formation. Water availability during the wet season is obviously sufficient to promote an initial feldspar breakdown and grus production, while the dry season restricts further clay development.

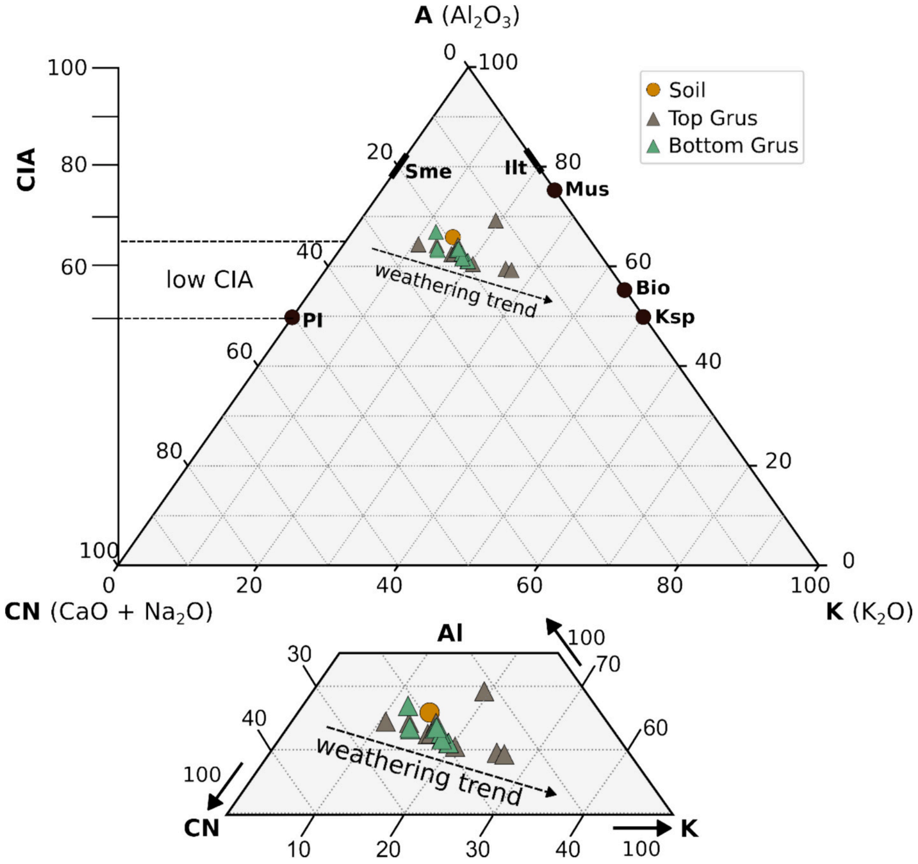

Fig. 9. A-CN-K ternary diagram of molecular proportions of Al_2O_3-($CaO^* + Na_2O$)-K_2O (Nesbitt and Young, 1984) together with the CIA scale along the A-CN side. The inner rectangle provides a detailed view of the data.

Table 2
Average geochemical compositions (wt%) and weathering indices of the top ($n = 10$) and bottom ($n = 9$) grus (with 1σ standard deviation — SD).

Samples	Top grus		Bottom grus	
	Average	SD (1σ)	Average	SD (1σ)
SiO_2	75.5	5.3	74.0	5.7
Al_2O_3	12.2	2.4	12.8	3.0
Fe_2O_3	2.3	0.7	2.7	0.6
CaO	0.9	0.4	1.1	0.3
MgO	0.6	0.3	0.7	0.3
Na_2O	2.8	1.1	3.1	1.0
K_2O	3.5	0.7	3.2	0.2
TiO_2	0.2	0.1	0.3	0.1
MnO	0.03	0.01	0.03	0.01
P_2O_5	0.1	0.04	0.1	0.04
LOI	1.9	1.1	2.1	1.2
Total	99.9	1.2	100.2	0.8
Rb	119.8	30.4	109.0	22.6
Ba	395.1	151.9	447.8	154.9
Eu	0.4	0.2	0.5	0.1
Ta	0.6	0.3	0.6	0.2
Th	5.1	1.2	5.9	2.1
U	1.8	0.4	2.0	0.6
$R^{3+}R^{2+}M^{+}$	530.7	106.3	556.0	117.8
$R^{3+}/R^{3+}R^{2+}M^{+}$	0.5	0.03	0.5	0.01
Δ4Si%	27.2	10.7	24.6	10.4
WIP	45.5	5.5	45.9	7.0
CIA	57.6	3.1	57.4	1.3
CIW	69.9	4.3	67.9	1.4
PIA	61.3	4.6	60.3	1.4

5.2. Weathering patterns and grain size control

The trace element compositions of grus deposits in the study area with lower LILE and REE compared to the UCC (Supplementary Data S2) further support the low to moderate weathering in the region. This depletion in elements such as Cs and Ba suggests the leaching of more mobile elements, yet the lack of significant clay mineral formation implies that chemical weathering has been insufficient to deeply alter the granite. These results are in line with findings from other granitoid regions, where moderate weathering led to the formation of a patchy grus cover rather than deeply weathered saprolite (e.g., Heimsath et al., 2012; Neely et al., 2019).

PCA revealed two key trends in the grus deposits (Fig. 11): PCA1 is primarily associated with the chemical composition of the samples, while PCA2 is mostly related to the grain size parameters (e.g., skewness, kurtosis). PCA1 shows a strong negative correlation with SiO_2 and positive correlations with Al_2O3, Fe_2O_3, CaO and MgO (Fig. 11), indicating that weathering has resulted in the enrichment of these elements. The higher concentration of Al, Fe, Ca and Mg in the grus samples indicates the breakdown of feldspar and biotite. In contrast, PCA2 highlights the importance of grain size, showing that finer, well-sorted top grus tends to have a higher SiO_2 content and more uniform grain size, reflecting less weathering. Coarser, poorly sorted bottom grus, however, is associated with higher concentrations of Al, Fe, and Mg, indicating more intense weathering in these areas. These results reflect the general weathering progression in granitoids, where coarser-grained material experienced more advanced weathering and contributes to the formation of thicker, heterogeneous grus layers in downslope areas.

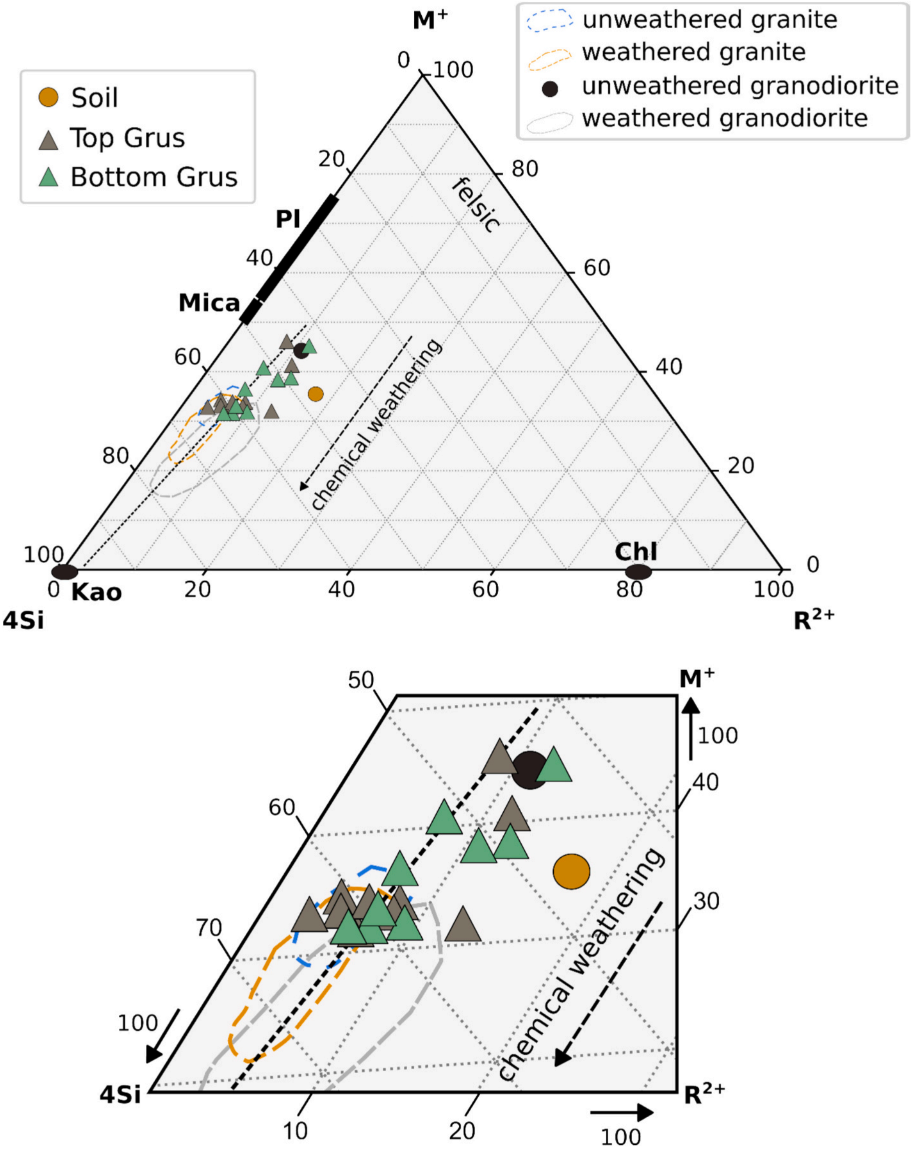

Fig. 10. Ternary diagram of the M^{+}-4Si-R^{2+} system. The weathering trends for granite (Meunier, 1980) and granodiorite (White et al., 2003) are delineated along with the field representing the average composition of felsic rocks (Condie, 1993). The panel below displays a detailed view of the data.

5.3. Relationship between grus weathering and climatic conditions

The implications of grus weathering for interpreting paleoenvironmental conditions may not be reliable, as many factors including topography and parent rock characteristics can significantly affect the physical and chemical characteristics of grus over time (Migoń, 1997; Migoń and Thomas, 2002). One of the most compelling findings of this study is the inference that alternating climatic conditions have played a significant role in controlling grus formation in the Mediterranean climate of the Çine submassif since the latest Miocene. Seasonal drought creates conditions favorable for the breakdown of granite, primarily through Fe oxidation in feldspar and biotite. The oxidative biotite weathering in granitoids, where Fe oxidation in biotite leads to volumetric expansion, results in matrix cracks that facilitate water infiltration and mineral dissolution (Buss et al., 2008; Goodfellow and Hilley, 2022). This process is particularly relevant in our context, where fractures and exfoliation surfaces (Fig. 2; Gül and Uslular, 2016) have enhanced grus formation by increasing rock susceptibility to weathering.

Our findings suggest that in the Mediterranean climate of region, grus formation is strongly limited by water availability. During the dry season, the limited water availability diminishes leaching, preventing the development of a more homogeneous clay-rich grus, while during the wet season, water infiltrates the rock, promoting chemical weathering. This cyclical process contributes to the formation of a heterogeneous weathering zone, with variability in mineral composition and grain size across both horizontal and vertical scales. Coarse-grained grus, which is less susceptible to weathering, dominates in areas of upper slopes, while finer, more weathered material accumulates in depressions or downslope regions, where transport processes are less pronounced. These observations align with similar findings in other granitoid regions, where variations in grus thickness are related to topographic features and climatic factors (Campbell and Twidale, 1995; Migoń and Thomas, 2002; Fletcher et al., 2006; Leonov et al., 2014; Scarciglia, 2015; Kajdas et al., 2017; Raab, 2019; Li et al., 2020; Raab et al., 2022; Goodfellow and Hilley, 2022). Thus, it can be concluded that the formation and spatial variability of grus mantles in granitoid regions are determined by structural, mineralogical and climatic properties (White and Brantley, 1995; Riebe et al., 2017; Goodfellow and Hilley, 2022).

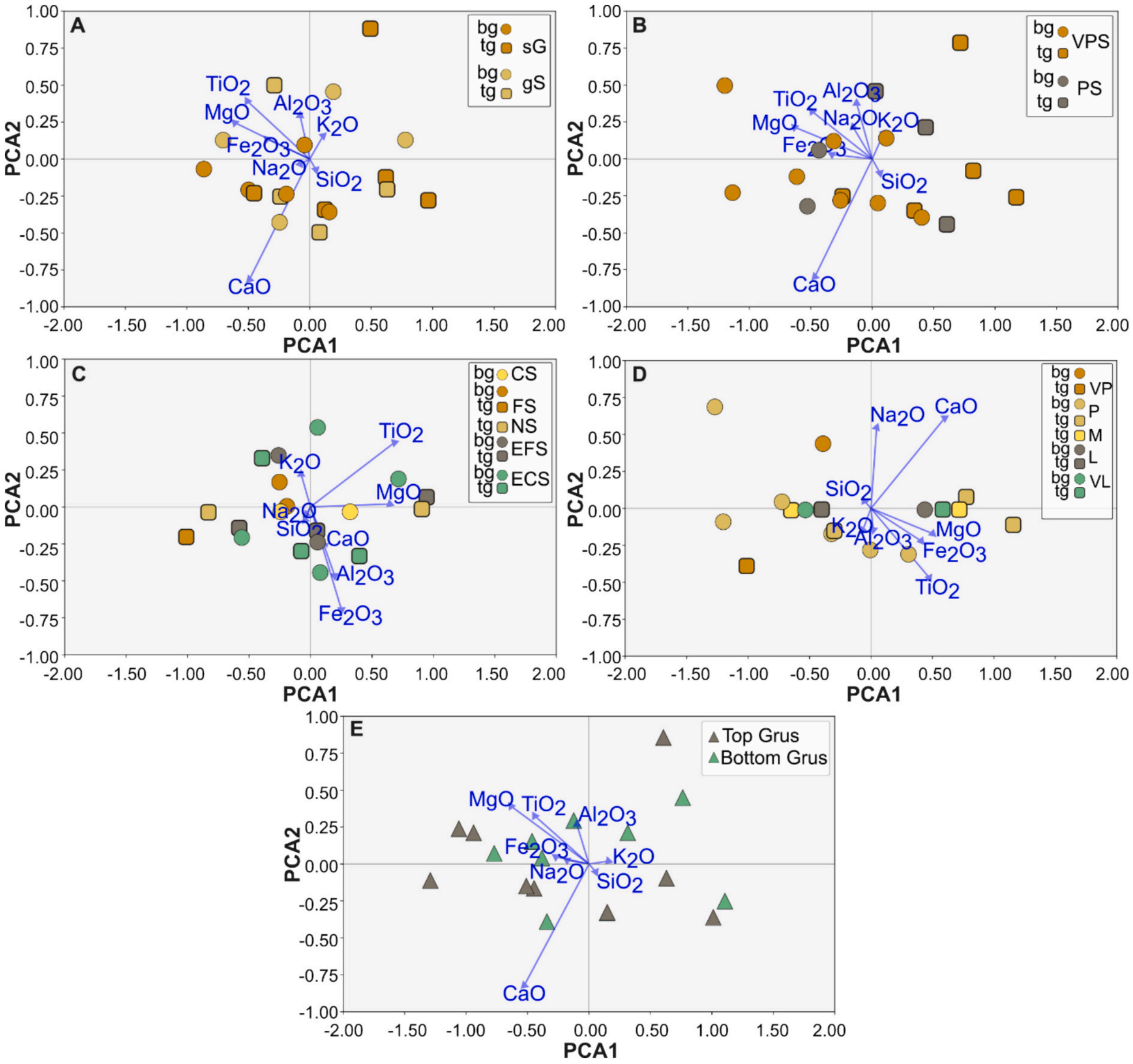

Fig. 11. PCA results of the grus samples for the Folk's sediment classification (A), different grain size parameters (B-D: sorting, skewness, and kurtosis, respectively), and the sample types (E). bg: bottom grus, tg: top grus, CS: coarse skewed, FS: fine skewed, NS: average skewed, EFS: extremely fine skewed, ECS: extremely coarse skewed, VPS: very poorly sorted, PS: poorly sorted, VP: very platykurtic, P: platykurtic, M: mesokurtic, L: leptokurtic, VL: very leptokurtic.

6. Conclusions

The grus deposits in the Çine submassif exhibit significant variability in their physical and chemical characteristics, influenced by topography, parent rock characteristics, and climatic conditions. Deposits are thinner and more homogeneous on upper slopes, while thicker and more heterogeneous grus accumulates in downslope areas and depressions, reflecting the combined effects of weathering intensity and transport processes. Grain size analyses highlight the predominance of poorly sorted sandy gravel, with finer, more uniform deposits in top grus layers and coarser, bimodal distributions in bottom layers. This variation in grain size not only reflects differential weathering and sorting but also indicates that change in weathering intensity and transport dynamics, influenced by alternating climatic conditions, have shaped the grus deposits over time.

Mineralogical and geochemical analyses reveal that the grus deposits are in an early to moderate stage of weathering, with feldspar and biotite transforming into illite, while secondary minerals such as kaolinite are limited. The weathering indices (e.g., CIA values between 59 and 59) further confirm moderate weathering, insufficient to generate deeply weathered grus. Trace element depletion (e.g., Cs, Ba, REEs) supports limited chemical weathering, consistent with episodic water availability in the Mediterranean climate.

We infer that the formation of grus is strongly controlled by alternating wet and dry climatic conditions, which influence mineral weathering and grain size distribution. Seasonal drought prevents leaching, while wet periods promote initial feldspar breakdown and grus production, resulting in a heterogeneous weathering profile. Topographic factors further contribute to the spatial variability of grus, with finer material accumulating in areas of reduced transport. Overall, the findings emphasise the importance of climatic variability, topography, and parent rock composition in shaping the characteristics of grus deposits, offering insights into weathering processes in Mediterranean granitoid environments.

Supplementary data to this article can be found online at https://doi.org/10.1016/j.geomorph.2025.109641.

CRediT authorship contribution statement

Murat Gül: Visualization, Validation, Supervision, Project

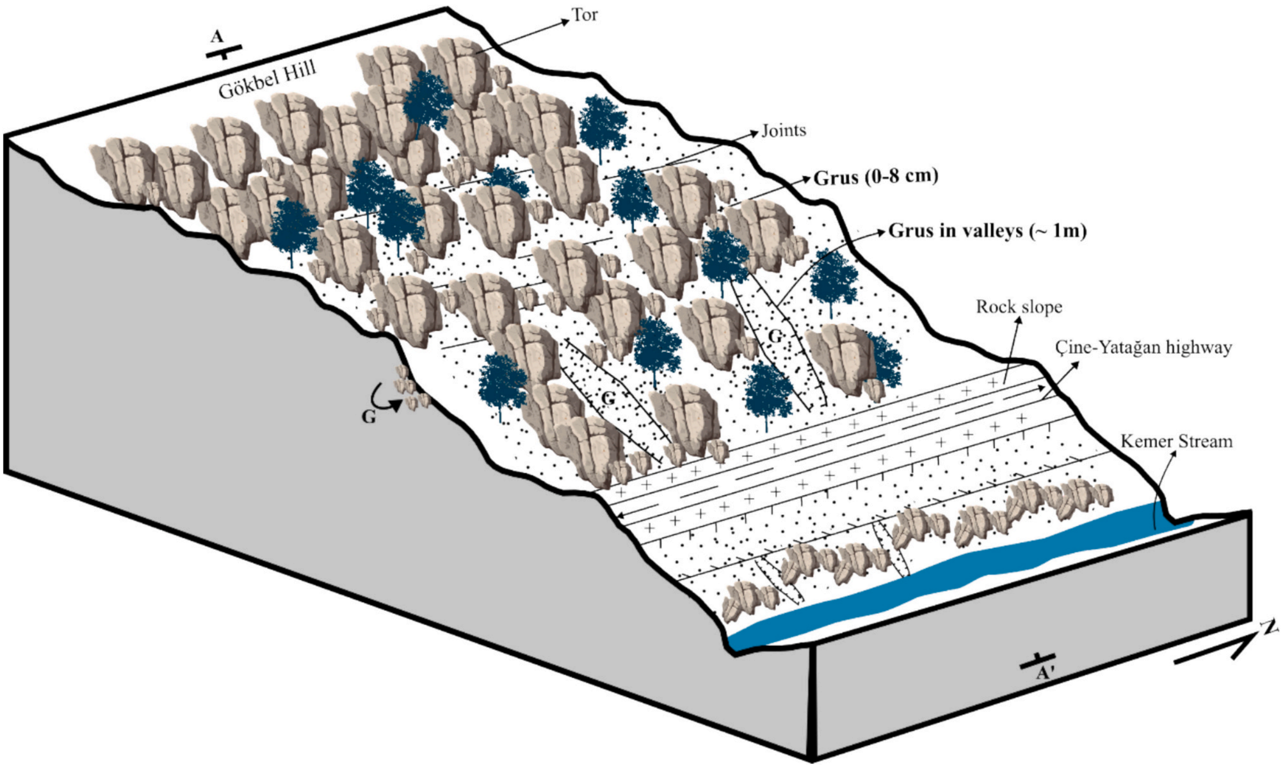

Fig. 12. Cross-sectional view of the grus formation in the Çine submassif, representing tors with fractures and exfoliation surfaces formed predominantly by regional metamorphic and tectonic processes in the region (i.e., exhumation, unroofing, uplifting, and extension), leading to the formation of grus deposits. This formation occurred in response to topographic variations, revealed by the different grus thickness and characteristics, during alternating periods of arid and humid climatic conditions (i.e., Mediterranean climate) from the Pliocene onwards.

administration, Methodology, Funding acquisition, Conceptualization, Writing – review & editing, Writing – original draft. **Ceren Küçükuysal:** Visualization, Resources, Methodology, Investigation, Data curation, Writing – review & editing, Writing – original draft. **Göksu Uslular:** Visualization, Software, Methodology, Formal analysis, Writing – review & editing, Writing – original draft. **Markus Egli:** Supervision, Writing – review & editing, Writing – original draft. **Gerald Raab:** Writing – review & editing, Writing – original draft.

Declaration of competing interest

The authors declare the following financial interests/personal relationships which may be considered as potential competing interests:

MG, CK, and GU report financial support was provided by Scientific and Technological Research Council of Turkey.

Acknowledgments

This study was supported by the Scientific and Technical Research Council of Türkiye (TÜBİTAK) with the grant number 121Y318. We thank Merve Gülcan for her kind assistance during field and laboratory studies. We would like to sincerely thank the editor Dr. Achim A. Beylich and the anonymous reviewers for their constructive feedback during the peer-review period. Special thanks to Reviewer 2 for their detailed and insightful comments, which have greatly helped in advancing the manuscript.

Data availability

This study used digital elevation models freely obtained from https://www.eorc.jaxa.jp/ALOS/en/dataset/aw3d30/aw3d30_e.htm. The Python scripts used for performing formal analyses (e.g., PCA, Genetic Algorithm) and creating plots are available by GU if requested.

References

Akgün, F., Kayseri, M.S., Akkiraz, M.S., 2007. Palaeoclimatic evolution and vegetational changes during the Late Oligocene–Miocene period in Western and Central Anatolia (Turkey). Palaeogeogr Palaeoclimatol Palaeoecol, Miocene Climate in Europe - patterns and evolution. First synthesis of NECLIME 253, 56–90. https://doi.org/10.1016/j.palaeo.2007.03.034.

Alçiçek, H., Jiménez-Moreno, G., 2013. Late Miocene to Plio-Pleistocene fluvio-lacustrine system in the Karacasu Basin (SW Anatolia, Turkey): Depositional, paleogeographic and paleoclimatic implications. Sediment. Geol. 291, 62–83. https://doi.org/10.1016/j.sedgeo.2013.03.014.

Alkanoğlu, E., 1984. Menderes masifindeki tafoniler. Yeryuvarı ve İnsan 8, 11–13 (in Turkish).

Biscaye, P.E., 1965. Mineralogy and Sedimentation of recent Deep-Sea Clay in the Atlantic Ocean and Adjacent Seas and Oceans. GSA Bull. 76, 803–832. https://doi.org/10.1130/0016-7606(1965)76[803:MASORD]2.0.CO;2.

Blott, S.J., Pye, K., 2001. GRADISTAT: a grain size distribution and statistics package for the analysis of unconsolidated sediments. Earth Surf. Process. Landf. 26, 1237–1248. https://doi.org/10.1002/esp.261.

Boski, T., Pessoa, J., Pedro, P., Thorez, J., Dias, J.M.A., Hall, I.R., 1998. Factors governing abundance of hydrolyzable amino acids in the sediments from the N.W. European Continental margin (47–50°N). Prog. Oceanogr. 42, 145–164. https://doi.org/10.1016/S0079-6611(98)00032-9.

Bozkurt, E., 2001. Neotectonics of Turkey: synthesis. Geodin. Acta 14, 3–30. https://doi.org/10.1080/09853111.2001.11432432.

Bozkurt, E., 2004. Granitoid rocks of the southern Menderes Massif (southwestern Turkey): Field evidence for Tertiary magmatism in an extensional shear zone. Int. J. Earth Sci. 93, 52–71. https://doi.org/10.1007/s00531-003-0369-0.

Bozkurt, E., Oberhänsli, R., 2001. Menderes Massif (Western Turkey): structural, metamorphic and magmatic evolution – a synthesis. Int. J. Earth Sci. 89, 679–708. https://doi.org/10.1007/s005310000173.

Bozkurt, E., Winchester, J.A., Park, R.G., 1995. Geochemistry and tectonic significance of augen gneisses from the southern Menderes Massif (West Turkey). Geol. Mag. 132, 287–301. https://doi.org/10.1017/S0016756800013613.

Brantley, S.L., Lebedeva, M., 2011. Learning to Read the Chemistry of Regolith to Understand the critical Zone. Annu. Rev. Earth Planet. Sci. 39, 387–416. https://doi.org/10.1146/annurev-earth-040809-152321.

Brindley, G.W., 1980. Quantitative X-ray Mineral Analysis of Clays, in: Brindley, G.W., Brown, G. (Eds.), Crystal Structures of Clay Minerals and their X-Ray Identification.

Mineralogical Society of Great Britain and Ireland, p. 0. doi:https://doi.org/10.1180/mono-5.7.

Brückner, H., Kelterbaum, D., Marunchak, O., Porotov, A., Vött, A., 2010. The Holocene sea level story since 7500 BP – Lessons from the Eastern Mediterranean, the Black and the Azov Seas. Quaternary International, Caspian–Black Sea–Mediterranean Corridors during the Last 30 ka: Sea Level Change and Human Adaptive. Strategies 225, 160–179. https://doi.org/10.1016/j.quaint.2008.11.016.

Buss, H.L., Sak, P.B., Webb, S.M., Brantley, S.L., 2008. Weathering of the Rio Blanco quartz diorite, Luquillo Mountains, Puerto Rico: Coupling oxidation, dissolution, and fracturing. Geochim. Cosmochim. Acta 72 (18), 4488–4507.

Campbell, E.M., Twidale, C.R., 1995. Lithologic and Climatic Convergence in Granite Morphology. Caderno Lab. Xeolóxicode Laxe Coruña 20, 381–403.

Candan, O., Dora, O., Oberhänsli, R., Çetinkaplan, M., Partzsch, J., Warkus, F., Dürr, S., 2001. Pan-African high-pressure metamorphism in the Precambrian basement of the Menderes Massif, western Anatolia, Turkey. Int. J. Earth Sci. 89, 793–811. https://doi.org/10.1007/s005310000097.

Candan, O., Koralay, O.E., Akal, C., Kaya, O., Oberhänsli, R., Dora, O.Ö., Konak, N., Chen, F., 2011. Supra-Pan-African unconformity between core and cover series of the Menderes Massif/Turkey and its geological implications. Precambrian Res. 184, 1–23. https://doi.org/10.1016/j.precamres.2010.09.010.

Chen, P.-Y., 1977. Table of Key Lines in X-Ray Powder Diffraction Patterns of Minerals in Clays and Associated Rocks, 67. Occasional Paper 21, Department of Natural Resources, Geological Survey, Bloomington.

Collins, A.S., Robertson, A.H.F., 1997. Lycian melange, southwestern Turkey: An emplaced late cretaceous accretionary complex. Geology 25, 255–258. https://doi.org/10.1130/0091-7613(1997)025<0255:LMSTAE>2.3.CO;2.

Condie, K.C., 1993. Chemical composition and evolution of the upper continental crust: Contrasting results from surface samples and shales. Chem. Geol. 104, 1–37. https://doi.org/10.1016/0009-2541(93)90140-E.

Darmody, R.G., Thorn, C.E., Seppälä, M., Campbell, S.W., Li, Y.K., Harbor, J., 2008. Age and weathering status of granite tors in Arctic Finland (68° N). Geomorphology 94, 10–23. https://doi.org/10.1016/j.geomorph.2007.04.006.

Dixon, J.L., von Blanckenburg, F., 2012. Soils as pacemakers and limiters of global silicate weathering. Compt. Rendus Geosci. 344, 597–609.

Egli, M., Nater, M., Mirabella, A., Raimondi, S., Plötze, M., Alioth, L., 2008. Clay minerals, oxyhydroxide formation, element leaching and humus development in volcanic soils. Geoderma 143, 101–114. https://doi.org/10.1016/j.geoderma.2007.10.020.

Fagel, N., Boski, T., Likhoshway, L., Oberhaensli, H., 2003. Late Quaternary clay mineral record in Central Lake Baikal (Academician Ridge, Siberia). Palaeogeogr. Palaeoclimatol. Palaeoecol. 193, 159–179. https://doi.org/10.1016/S0031-0182(02)00633-8.

Fedo, C.M., Nesbitt, H.W., Young, G.M., 1995. Unraveling the effects of potassium metasomatism in sedimentary rocks and paleosols, with implications for paleoweathering conditions and provenance. Geology 23, 921–924.

Fletcher, R., Buss, H., Brantley, S., 2006. A spheroidal weathering model coupling porewater chemistry to soil thicknesses during steady-state denudation. Earth Planet. Sci. Lett. 244, 444–457. https://doi.org/10.1016/j.epsl.2006.01.055.

Folk, R.L., 1954. The Distinction between grain size and Mineral Composition in Sedimentary-Rock Nomenclature. J. Geol. 62, 344–359. https://doi.org/10.1086/626171.

Garzanti, E., Padoan, M., Setti, M., López-Galindo, A., Villa, I.M., 2014. Provenance versus weathering control on the composition of tropical river mud (southern Africa). Chem. Geol. 366, 61–74. https://doi.org/10.1016/j.chemgeo.2013.12.016.

Gessner, K., Gallardo, L.A., Markwitz, V., Ring, U., Thomson, S.N., 2013. What caused the denudation of the Menderes Massif: Review of crustal evolution, lithosphere structure, and dynamic topography in Southwest Turkey. Gondwana Res. 24, 243–274. https://doi.org/10.1016/j.gr.2013.01.005.

Goodfellow, B.W., Hilley, G.E., 2022. Climatic and lithological controls on the structure and thickness of granitic weathering zones. Earth Planet. Sci. Lett. 600, 117890. https://doi.org/10.1016/j.epsl.2022.117890.

Goodfellow, B.W., Hilley, G.E., Schulz, M.S., 2011. Vadose zone controls on weathering intensity and depth: Observations from grussic saprolites. Appl. Geochem. 26, 36–39.

Goodfellow, B.W., Chadwick, O.A., Hilley, G.E., 2014. Depth and character of rock weathering across a basaltic-hosted climosequence on Hawai 'i. Earth Surf. Process. Landf. 39 (3), 381–398.

Gül, M., Uslular, G., 2016. Geomorphological features and weathering of the Southern Submassif of the Menderes Massif (SW Turkey). Arab. J. Geosci. 9, 682. https://doi.org/10.1007/s12517-016-2715-0.

Gürer, Ö., Yılmaz, Y., 2002. Geology of the Ören and Surrounding areas, SW Anatolia. Turk. J. Earth Sci. 11, 1–13.

Gürer, Ö.F., Sanğu, E., Özburan, M., Gürbüz, A., Sarica-Filoreau, N., 2013. Complex basin evolution in the Gökova Gulf region: implications on the late Cenozoic tectonics of Southwest Turkey. Int. J. Earth Sci. (Geol. Rundsch.) 102, 2199–2221. https://doi.org/10.1007/s00531-013-0909-1.

Gürsu, S., 2016. A new petrogenetic model for meta-granitic rocks in the central and southern Menderes Massif – W Turkey: Implications for Cadomian crustal evolution within the Pan-African mega-cycle. Precambrian Res. 275, 450–470. https://doi.org/10.1016/j.precamres.2016.01.025.

Harnois, L., 1988. The CIW index: a new chemical index of weathering. Sediment. Geol. 55, 319–322. https://doi.org/10.1016/0037-0738(88)90137-6.

Hayes, N.R., Buss, H.L., Moore, O.W., Krám, P., Pancost, R.D., 2020. Controls on granitic weathering fronts in contrasting climates. Chem. Geol. 535, 119450. https://doi.org/10.1016/j.chemgeo.2019.119450.

Heimsath, A.M., DiBiase, R.A., Whipple, K.X., 2012. Soil production limits and the transition to bedrock-dominated landscapes. Nat. Geosci. 5 (3), 210–214.

Irfan, T.Y., 1996. Mineralogy, fabric properties and classification of weathered granites in Hong Kong. Q. J. Eng. Geol. 29, 5–35. https://doi.org/10.1144/GSL.QJEGH.1996.029.P1.02.

Jenny, H., 1942. Calcium in the soil: III. Pedologic Relations. Soil Sci. Soc. Am. J. 6, 27–35.

Jiménez-Moreno, G., Alçiçek, H., Alçiçek, M.C., Ostende, L. van den H., Wesselingh, F.P., 2015. Vegetation and climate changes during the late Pliocene and early Pleistocene in SW Anatolia, Turkey. Quat. Res. 84, 448–456. https://doi.org/10.1016/j.yqres.2015.09.005.

Kajdas, B., Michalik, M.J., Migoń, P., 2017. Mechanisms of granite alteration into grus, Karkonosze granite, SW Poland. Catena (Amst) 150, 230–245. https://doi.org/10.1016/j.catena.2016.11.026.

Kanamaru, T., Suganuma, Y., Oiwane, H., Miura, H., Miura, M., Okuno, J., Hayakawa, H., 2018. The weathering of granitic rocks in a hyper-arid and hypothermal environment: a case study from the Sør-Rondane Mountains, East Antarctica. Geomorphology 317, 62–74. https://doi.org/10.1016/j.geomorph.2018.05.015.

Kayseri, M.S., Akgün, F., 2010. Türkiye'de Geç Burdigaliyen-Langiyen Periyodu ve Avrupa ile Paleortamsal ve Paleoiklimsel Karşılaştırma: Muğla-Milas (Kultak) Langiyen Palinoflorası ve Paleoiklimsel Özellikleri. Geol. Bull. Turkey 53 (1), 1–44 (in Turkish with English abstract).

Kayseri-Özer, M.S., 2013. Spatial distribution of climatic conditions from the Middle Eocene to late Miocene based on palynoflora in Central, Eastern and Western Anatolia. Geodin. Acta 26, 122–157. https://doi.org/10.1080/09853111.2013.877237.

Koralay, O.E., Candan, O., Chen, F., Akal, C., Oberhänsli, R., Satır, M., Dora, O.Ö., 2012. Pan-African magmatism in the Menderes Massif: geochronological data from leucocratic tourmaline orthogneisses in western Turkey. Int. J. Earth Sci. (Geol. Rundsch.) 101, 2055–2081. https://doi.org/10.1007/s00531-012-0775-2.

Le Pera, E., Sorriso-Valvo, M., 2000. Weathering and morphogenesis in a mediterranean climate, Calabria, Italy. Geomorphology 34, 251–270. https://doi.org/10.1016/S0169-555X(00)00012-X.

Leonov, M.G., Tsekhovskii, Yu.G., Przhiyalgovskii, E.S., Poleshchuk, A.V., Lavrushina, E. V., 2014. Polygenic nature of granite clastites: Communication 1. Exogenic and tectonic postmagmatic disintegration of granite massifs. Lithol. Miner. Resour. 49, 81–102. https://doi.org/10.1134/S0024490213060060.

Li, C., Kong, L., Shu, R., An, R., Zhang, X., 2020. Disintegration characteristics in granite residual soil and their relationship with the collapsing gully in South China. Open Geosci. 12, 1116–1126. https://doi.org/10.1515/geo-2020-0178.

McLennan, S.M., 1993. Weathering and Global Denudation. J. Geol. 101, 295–303. https://doi.org/10.1086/648222.

Mersin, D., Gulmez, A., Safari, M.J.S., Vaheddoost, B., Tayfur, G., 2022. Drought Assessment in the Aegean Region of Turkey. Pure Appl. Geophys. 179, 3035–3053. https://doi.org/10.1007/s00024-022-03089-7.

Meunier, A., 1980. Les mecanismes de l'alteration des granites et le role des microsystemes. Etude des arenes du massif granitique de Parthenay (Deux-Sevres). Soc. Géol. Fr. Mém. 140, 1–80.

Meunier, A., Caner, L., Hubert, F., El Albani, A., Prêt, D., 2013. The weathering intensity scale (WIS): An alternative approach of the chemical index of alteration (CIA). Am. J. Sci. 313, 113–143.

Migoń, P., 1997. Palaeoenvironmental Significance of grus Weathering Profiles: A Review with Special Reference to Northern and Central Europe. Proc. Geol. Assoc. 108 (1), 57–70.

Migoń, P., 2022. 3.14 - Weathering and Hillslope Development. In: Shroder, J., (Jack) F. (Eds.), Treatise on Geomorphology, Second edition. Academic Press, Oxford, pp. 236–257. https://doi.org/10.1016/B978-0-12-818234-5.00215-7.

Migoń, P., Thomas, M.F., 2002. Grus weathering mantles—problems of interpretation. Catena (Amst). The interpretation and significance of weathering mantels 49, 5–24. https://doi.org/10.1016/S0341-8162(02)00014-0.

Migoń, P., Vieira, G., 2014. Granite geomorphology and its geological controls, Serra da Estrela, Portugal. Geomorphology 226, 1–14. https://doi.org/10.1016/j.geomorph.2014.07.027.

Moignien, R., 1966. Review of Research on Laterites. Natural Resources Research IV. United Nations Educational Scientific and Cultural Organization (UNESCO), Vaillant-Carmanne, Liège, p. 148.

Moore, D.M., Reynolds, J., 1989. X-Ray Diffraction and the Identification and Analysis of Clay Minerals. Oxford University Press, New York, p. 322.

Müllenhoff, M., Handl, M., Knipping, M., Brückner, H., 2004. The evolution of Lake Bafa (Western Turkey) – Sedimentological, microfaunal and palynological results. Coastline Rep. ISSN: 0928-2734 1, 55–66.

Navarre-Sitchler, A., Brantley, S.L., Rother, G., 2015. How porosity increases during incipient weathering of crystalline silicate rocks. Rev. Mineral. Geochem. 80, 331–354.

Neely, A.B., DiBiase, R.A., Corbett, L.B., Bierman, P.R., Caffee, M.W., 2019. Bedrock fracture density controls on hillslope erodibility in steep, rocky landscapes with patchy soil cover, southern California, USA. Earth Planet. Sci. Lett. 522, 186–197.

Nesbitt, H.W., Young, G.M., 1984. Prediction of some weathering trends of plutonic and volcanic rocks based on thermodynamic and kinetic considerations. Geochim. Cosmochim. Acta 48, 1523–1534.

Nesbitt, Hw, Young, G.M., 1982. Early Proterozoic climates and plate motions inferred from major element chemistry of lutites. Nature 299, 715–717.

Ng, C.W.W., Guan, P., Shang, Y.J., 2001. Weathering mechanisms and indices of the igneous rocks of Hong Kong. Q. J. Eng. Geol. Hydrogeol. 34, 133–151. https://doi.org/10.1144/qjegh.34.2.133.

Ocakoğlu, F., 2020. Rapid late Quaternary denudation of the Karacasu Graben in response to subsidence in the Büyük Menderes Corridor: Insights from morphotectonics and archaeogeology. Geomorphology 357. https://doi.org/10.1016/j.geomorph.2020.107107.

Özer, S., Sözbilir, H., Özkar, İ., Toker, V., Sari, B., 2001. Stratigraphy of Upper Cretaceous–Palaeogene sequences in the southern and eastern Menderes Massif (western Turkey). Int. J. Earth Sci. 89, 852–866. https://doi.org/10.1007/s005310000142.

Parker, A., 1970. An index of weathering for silicate rocks. Geol. Mag. 101, 501–504.

Pedregosa, F., Varoquaux, G., Gramfort, A., Michel, V., Thirion, B., Grisel, O., Blondel, M., Prettenhofer, P., Weiss, R., Dubourg, V., Vanderplas, J., Passos, A., Cournapeau, D., Brucher, M., Perrot, M., Duchesnay, E., 2011. Scikit-Learn: Machine Learning in Python. J. Mach. Learn. Res. 12, 2825–2830.

Price, J.R., Velbel, M.A., 2003. Chemical weathering indices applied to weathering profiles developed on heterogeneous felsic metamorphic parent rocks. Chem. Geol. 202, 397–416. https://doi.org/10.1016/j.chemgeo.2002.11.001.

Raab, G., 2019. "The" Tor Exhumation Approach: A New Technique to Derive Continuous in Situ Soil Erosion and Surface Denudation Models (Doctorate). Universitat Zurich, Zurich.

Raab, G., Halpern, D., Scarciglia, F., Raimondi, S., Norton, K., Pettke, T., Hermann, J., de Castro Portes, R., Sanchez, A.M.A., Egli, M., 2017. Linking tephrochronology and soil characteristics in the Sila and Nebrodi mountains, Italy. Catena (Amst) 158, 266–285.

Raab, G., Egli, M., Norton, K.P., Martin, A.P., Ketterer, M.E., Tikhomirov, D., Wanner, R., Scarciglia, F., 2022. Soil weathering dynamics and erosion in a dry oceanic area of the southern hemisphere (Otago, New Zealand). Sci. Rep. 12, 19803. https://doi.org/10.1038/s41598-022-23731-7.

Régnier, J.L., Mezger, J.E., Passchier, C.W., 2007. Metamorphism of Precambrian-Palaeozoic schists of the Menderes core series and contact relationships with Proterozoic orthogneisses of the western Çine Massif, Anatolide belt, western Turkey. Geol. Mag. 144, 67–104. https://doi.org/10.1017/S0016756806002640.

Riebe, C.S., Hahm, W.J., Brantley, S.L., 2017. Controls on deep critical zone architecture: a historical review and four testable hypotheses. Earth Surf. Process. Landf. 42, 128–156. https://doi.org/10.1002/esp.4052.

Rimmelé, G., Parra, T., Goffé, B., Oberhänsli, R., Jolivet, L., Candan, O., 2005. Exhumation paths of high-pressure - Low-temperature metamorphic rocks from the Lycian Nappes and the Menderes Massif (SW Turkey): a multi-equilibrium approach. J. Petrol. 46, 641–669. https://doi.org/10.1093/petrology/egh092.

Ruxton, B.P., 1968. Measures of the Degree of Chemical Weathering of Rocks. Source: J. Geol. 76 (5), 518–527.

Scarciglia, F., 2015. Weathering and exhumation history of the Sila Massif upland plateaus, southern Italy: a geomorphological and pedological perspective. J. Soils Sediments 15, 1278–1291. https://doi.org/10.1007/s11368-014-0923-3.

Şengör, A.M.C., Satir, M., Akkök, R., 1984. Timing of Tectonic events in the Menderes Massif, Western Turkey: Implications for Tectonic Evolution and evidence for Pan-African Basement in Turkey. Tectonics 3, 693–707.

Sheldon, N.D., Tabor, N.J., 2009. Quantitative paleoenvironmental and paleoclimatic reconstruction using paleosols. Earth Sci. Rev. 95 (1–2), 1–52. https://doi.org/10.1016/j.earscirev.2009.03.004.

Shen, X., Arson, C., Ferrier, K.L., West, N., Dai, S., 2019. Mineral Weathering and Bedrock weakening: Modeling Microscale Bedrock damage under Biotite Weathering. JGR Earth Surface 124, 2623–2646. https://doi.org/10.1029/2019JF005068.

Tadono, T., Takaku, J., Tsutsui, K., Oda, F., Nagai, H., 2015. Status of "ALOS World 3D (AW3D)" global DSM generation. International Geoscience and Remote Sensing Symposium (IGARSS). 3822–3825. https://doi.org/10.1109/IGARSS.2015.7326657.

Taylor, S.R., McLennan, S.M., 1985. The Continental Crust: Its Composition and Evolution. Blackwell, Oxford, UK, p. 349.

Thorez, J., 1976. Practical Identification of Clay Minerals : A Handbook for Teachers and Students in Clay Mineralogy, (no Title). Liege State University, Belgium, Institute of Mineralogy.

Twidale, C.R., 1986. Granite landform evolution: Factors and implications. Geol. Rundsch. 75, 769–779. https://doi.org/10.1007/BF01820646.

Twidale, C.R., 1997. Some recently developed landforms: climatic implications. Geomorphology, Geomorphic responses to short-term climatic change 19, 349–365. https://doi.org/10.1016/S0169-555X(97)00019-6.

van Hinsbergen, D.J.J., 2010. A key extensional metamorphic complex reviewed and restored: the Menderes Massif of western Turkey. Earth Sci. Rev. 102 (1–2), 60–76. https://doi.org/10.1016/j.earscirev.2010.05.005.

Vogel, D.E., 1975. Precambrian Weathering in Acid Metavolcanic Rocks from the Superior Province, Villebon Township, South-Central Québec. Can. J. Earth Sci. 12, 2080–2085. https://doi.org/10.1139/e75-183.

Vogt, T., 1927. Sulitjelmefeltets geologiog petrografi. Norges Geologiske Undersokelse 121, 1–560 (In Norwegian, with English Abstract).

Weber, J., Tyszka, R., Kocowicz, A., Szadorski, J., Debicka, M., Jamroz, E., 2012. Mineralogical composition of the clay fraction of soils derived from granitoids of the Sudetes and Fore-Sudetic Block, Southwest Poland. Eur. J. Soil Sci. 63 (5), 762–772.

Westaway, R., Pringle, M., Yurtmen, S., Demir, T., Bridgland, D., Rowbotham, G., Maddy, D., 2003. Pliocene and Quaternary surface uplift of western Turkey revealed by long-term river terrace sequences. Curr. Sci. 84, 1090–1101.

Westaway, R., Pringle, M., Yurtmen, S., Demir, T., Bridgland, D., Rowbotham, G., Maddy, D., 2004. Pliocene and Quaternary regional uplift in western Turkey: the Gediz River terrace staircase and the volcanism at Kula. Tectonophysics 391, 121–169. https://doi.org/10.1016/j.tecto.2004.07.013.

White, A.F., Brantley, S.L., 1995. Chemical Weathering rates of Silicate Minerals. De Gruyter, Berlin. https://doi.org/10.1515/9781501509650.

White, C.E., Barr, S.M., Miller, B.V., Hamilton, M.A., 2003. Granitoid plutons of the Brookville terrane, southern New Brunswick: petrology, age, and tectonic setting. Atl. Geol. 38 (1), 53–74. https://doi.org/10.4138/1255.

Whitney, D.L., Bozkurt, E., 2002. Metamorphic history of the southern Menderes massif, western Turkey. GSA Bull. 114, 829–838. https://doi.org/10.1130/0016-7606(2002)114<0829:MHOTSM>2.0.CO;2.

Xu, T., Shen, X., Reed, M., West, N., Ferrier, K.L., Arson, C., 2022. Anisotropy and Microcrack Propagation Induced by Weathering, Regional Stresses and Topographic Stresses. JGR Solid. Earth 127, e2022JB024518. https://doi.org/10.1029/2022JB024518.